

Copyright
by
Sarah Yvonne Greer
2018

The Thesis committee for Sarah Yvonne Greer
Certificates that this is the approved version of the following thesis:

**A data matching algorithm and its applications in seismic
data analysis**

APPROVED BY

SUPERVISING COMMITTEE:

Dr. Sergey Fomel, Supervisor

Dr. Kyle Spikes

Dr. Clark Wilson

**A data matching algorithm and its applications in seismic
data analysis**

by

Sarah Yvonne Greer

THESIS

Presented to the Faculty of
The University of Texas at Austin
in Partial Fulfillment
of the Requirements
for the Degree of

BACHELOR OF SCIENCE

THE UNIVERSITY OF TEXAS AT AUSTIN

May 2018

Acknowledgments

Add acknowledgements here :)

A data matching algorithm and its applications in seismic data analysis

Sarah Yvonne Greer, B.S.

The University of Texas at Austin, 2018

Supervisor: Dr. Sergey Fomel

Abstract

Table of Contents

Acknowledgments	iv
Abstract	v
List of Tables	vii
List of Figures	viii
Chapter 1. Introduction	1
Chapter 2. Balancing local frequency content in seismic data using non-stationary smoothing	2
Chapter 3. Matching and merging high-resolution and legacy seismic images	16
Chapter 4. Improving migration resolution by approximating the least-squares Hessian using non-stationary amplitude and frequency matching	39
Chapter 5. Conclusions	52
Bibliography	53

List of Tables

List of Figures

2.1	Initial legacy (a) and high-resolution (b) images. These images show the same subsurface geology, but look remarkably different as the high-resolution image has distinctly higher frequency content than the legacy image.	7
2.2	The smoothing radius, which is a function of time and space, this method produces after 5 iterations. This represents the number of samples in time that the high-resolution image needs to be smoothed over in a triangle weight to balance local frequency content with the legacy image.	8
2.3	Spectral content of the legacy (red) and high-resolution (blue) images before (a) and after (b) spectral balancing.	10
2.4	Difference in local frequencies (residual) between the legacy and high-resolution images before (a) and after (b) the 5th iteration of frequency balancing.	12
2.5	Initial PP (a) and SS (b) images.	14
2.6	Interleaved PP and warped SS traces before (a) and after (b) frequency balancing and residual registration. After registration, the signal content between the two initial images is more aligned; for example, the reflections around 0.3 and 0.6 s. This indicates a successful registration.	15
3.1	The initial legacy (a) and high-resolution (b) images. The merged image (c) is the final product of the proposed workflow: the combination of both the legacy and high-resolution images.	19
3.2	Spectra for the entire image display of the legacy (red) and high-resolution (blue) images before (a) and after (b) spectral balancing.	21
3.3	Calculated spatially and temporally variable smoothing radius. This represents the number of seconds in the temporal direction that the high-resolution image gets averaged over in a triangle weight to balance local frequency content with the legacy image at each sample.	23
3.4	Difference in local frequencies between the legacy and high-resolution images before (a) and after (b) balancing their frequency content by non-stationary smoothing.	25

3.5	Difference between the legacy and smoothed high-resolution images before (a) and after (b) aligning the data sets. Before accounting for time shifts, much of the signal content did not align in time, so coherent reflections were subtracted out. After accounting for time shifts, the reflections are more aligned, so much of the subtracted information is noise.	27
3.6	The weights for the high-resolution (a) and legacy (b) images for the least-squares merge. The high-resolution weight is strongly weighted in the shallow part and blends to favor the legacy image with depth. The legacy weight is selected to boost the legacy image's relative amplitudes to match that of the high-resolution image.	29
3.7	The spectra of the entire image display of the legacy (red dashed), high-resolution (blue dotted), and merged (magenta solid) images for the first data set.	30
3.8	The first 600 ms of data from a sample line from the legacy, high-resolution, and merged image (a). The same images with depth for the legacy, high-resolution, and merged images (b). The merged image resembles the high-resolution image in the shallow parts and incorporates the more coherent lower frequency information from the legacy image with depth.	32
3.9	The spectral content of the entire image display of the legacy (red dashed), high-resolution (blue dotted), and resultant merged (magenta solid) images for the second data set.	36
3.10	The legacy (a), high-resolution (b), and resultant merged (c) images of the second data set.	37
4.1	The Sigsbee model reflectivity (a), migration velocity model (b), the first migrated image, \mathbf{m}_0 (c), and the second migrated image, \mathbf{m}_1 (d).	43
4.2	The forward amplitude balancing weight, \mathbf{A} (a) and the smoothing radius (b), which represents the number of samples in both dimensions that \mathbf{m}_0 must be smoothed over in a triangle weight to balance the local frequency content with \mathbf{m}_1 . This represents the forward smoothing operation, \mathbf{S}	46
4.3	The corrected migrated image, found by applying equation (4.10) to \mathbf{m}_0	48
4.4	The Sigsbee model reflectivity (a), the first migrated image (b), and the corrected migrated image (c).	49

Chapter 1

Introduction

Data matching is a conceptually simple problem that is present in many computational geophysics applications. Essentially, given two data sets, data matching can be thought of as finding the transformation from one data set to the other. This is useful in applications such as multi-component seismic image registration, where two separate seismic images, one P-wave image and one S- wave image, are acquired over the same area. These must be properly matched, as the two images are not temporally aligned and have different frequency and amplitude content, in order for them to be directly compared and interpreted.

Background

Seismic data contains fundamentally non-stationary variations.

Chapter 2

Balancing local frequency content in seismic data using non-stationary smoothing

Seismic data can experience non-stationary frequency variations caused by attenuation. This problem is encountered when matching multiple data sets, such as in multicomponent image registration, because signals with differing frequency content are hard to correlate. In this paper, we propose a method to balance frequency content between data sets while taking into account non-stationary frequency variations. This method involves finding and applying a non-stationary smoothing operator to minimize the local frequency difference between data sets. Numerical examples demonstrate that the proposed method improves multicomponent image registration and matching images of differing resolution.

INTRODUCTION

Matching seismic data has many applications in geophysical processing methods, such as multi-component image registration, time-lapse image registration, matching well-ties to seismic data, and merging seismic data sets (Ursenbach et al., 2013; Fomel and Backus, 2003a; Lumley et al., 2003; Herrera and van der Baan, 2012). Typically, the workflow for matching data involves finding the optimal time shift, or amount of stretching and compressing, of one trace relative to the other that produces the greatest similarity between the two traces, as seen in dynamic time warping and local

similarity scanning (Hale, 2013; Fomel and Jin, 2009; Herrera et al., 2014). However, when the two signals that need to be aligned have different spectral content, their comparison can be difficult. Most seismic data experience non-stationary, or spatially and temporally variant, frequency content caused by attenuation. This problem was discussed in application to multicomponent image registration by Fomel and Backus (2003a), who applied frequency balancing methods to improve registration results. Liu and Fomel (2012) proposed using local time-frequency decomposition (LTFD) to balance frequencies between multicomponent data during registration. However, LTFD is a relatively computationally expensive method.

In this paper, we propose a method to remove non-stationary frequency differences that limit the effectiveness of matching data. We suggest applying the proposed method to processing flows that involve matching data before attempting to find the time shift to align their signal content. To balance frequency content, we use a non-stationary smoothing operator with an adjustable smoothing radius to apply to the higher frequency data set. Our approach takes the form of an optimization problem which is solved using an iterative method. We apply this method to examples of merging high-resolution and conventional seismic images and multicomponent image registration.

METHOD

Two signals of differing frequencies are more difficult to correlate than signals of similar frequencies. For example, Figure 2.1 shows two seismic images representing the same subsurface, except they have distinctly different spectral content, as shown in Figure 2.3(a). In order to be directly comparable, these two images should have similar frequency content. In this paper, we look at local frequency (Fomel, 2007a),

which can be thought of as a smoothed estimate of instantaneous frequency (White, 1991). Local frequency is a more geologically accurate attribute than instantaneous frequency because it honors time-frequency uncertainty and does not contain physically unrealistic negative or extremely high frequency values (Fomel, 2007a).

In order to balance local frequency content, we propose smoothing the higher frequency data using a non-stationary triangle smoothing operator with an adjustable radius. Here, the radius at each point is the number of samples in time that that specific data point gets averaged over in a triangle weight.

Our goal is to find the temporally and spatially variable smoothing radius, \mathbf{R} , that minimizes the difference in local frequencies between the two data sets. This can be shown in the objective function

$$\min_{\mathbf{R} \in [1, N]} \left\| \mathbf{F}[\mathbf{S}_{\mathbf{R}} \mathbf{d}_h] - \mathbf{F}[\mathbf{d}_l] \right\|, \quad (2.1)$$

where $\mathbf{S}_{\mathbf{R}}$ is the non-stationary smoothing operator of smoothing radius \mathbf{R} , \mathbf{d}_h is the higher frequency data, \mathbf{d}_l is the lower frequency data, \mathbf{F} is the local frequency operator, and N is the maximum size of the smoothing radius. Although smoothing is a linear operation, the smoothed data, $\mathbf{S}_{\mathbf{R}} \mathbf{d}_h$, depends non-linearly on R . However, the objective from equation (2.1) is nearly convex, and we choose to use an intuitive iterative approach to find an approximate smoothing radius.

The main premise behind the method comes from the fact that, in general, the greater the smoothing radius, the more high frequencies are attenuated by smoothing. We choose an initial guess of the non-stationary smoothing radius before applying corrections based on two primary assumptions:

1. The smoothing radius is too *small* at a specified point if, after smoothing, the

higher frequency data has *higher* local frequency than the lower frequency data.

Thus, the smoothing radius must be *increased* at that point.

2. The smoothing radius is too *large* at a specified point if, after smoothing, the higher frequency data has *lower* local frequency than the lower frequency data. Thus, the smoothing radius must be *decreased* at that point.

We apply these assumptions using a line-search method:

$$\mathbf{R}^{(i+1)} = \mathbf{R}^{(i)} + \alpha \mathbf{r}^{(i)}, \quad (2.2)$$

where $\mathbf{R}^{(i)}$ is the smoothing radius at the i th iteration, α is a scalar constant that can be thought of as the step length, and $\mathbf{r}^{(i)}$ is the residual at the i th iteration, which can be thought of as the search direction, and is defined as

$$\mathbf{r} = \mathbf{F}[\mathbf{S}_\mathbf{R} \mathbf{d}_h] - \mathbf{F}[\mathbf{d}_l]. \quad (2.3)$$

It can be noted that when equation (3.11) is positive, the higher frequency data still has a higher local frequency value at that specific point than the lower frequency data, thus the higher frequency data is under-smoothed and the smoothing radius should be increased at that point. This follows the form of the first assumption. The second assumption is used when equation (3.11) is negative. When equation (3.11) is zero, the correct radius has been found and no further corrections are made. Thus, it is justifiable to set the search direction from equation (4.2) equal to the residual.

Using the two assumptions, we can continually adjust the smoothing radius until we achieve the desired result of balancing the local frequency content between the two data sets. In practice, this method produces an acceptable solution in approximately 5 iterations and exhibits sublinear convergence. After smoothing the higher

frequency data with the estimated radius, we use the lower frequency and smoothed higher frequency data to estimate time shifts and align the two data sets.

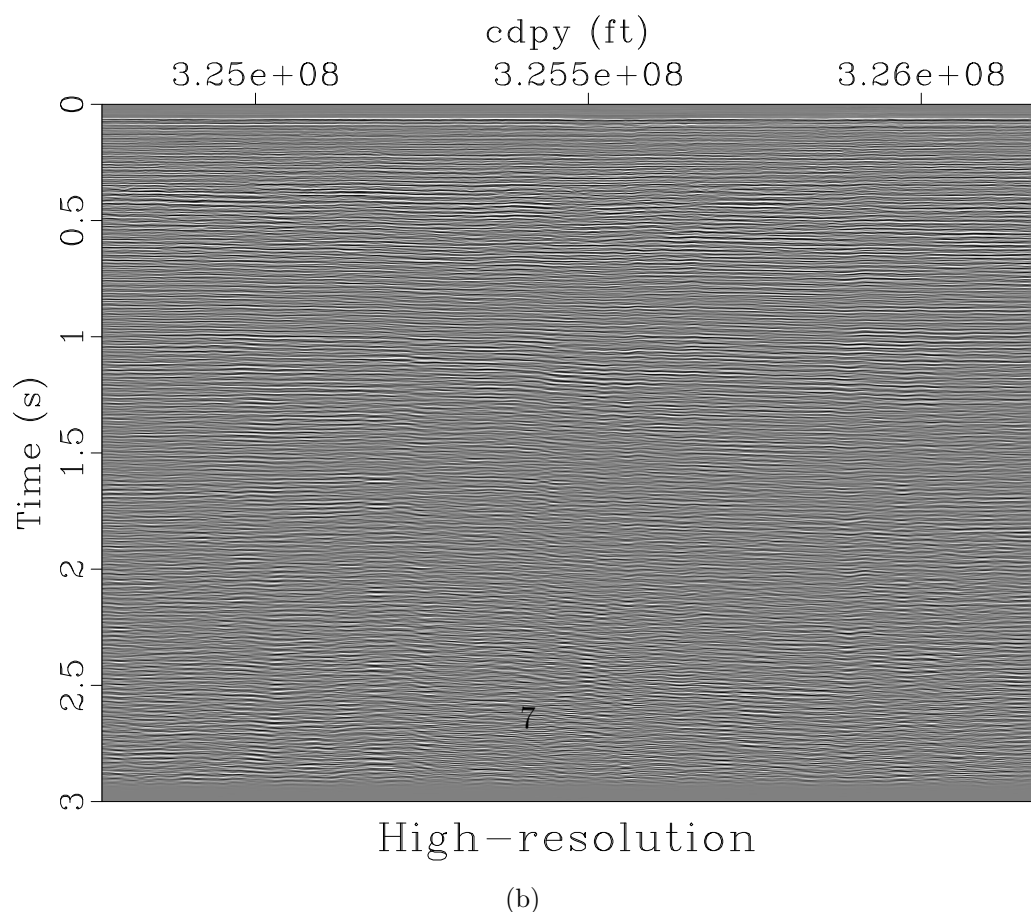
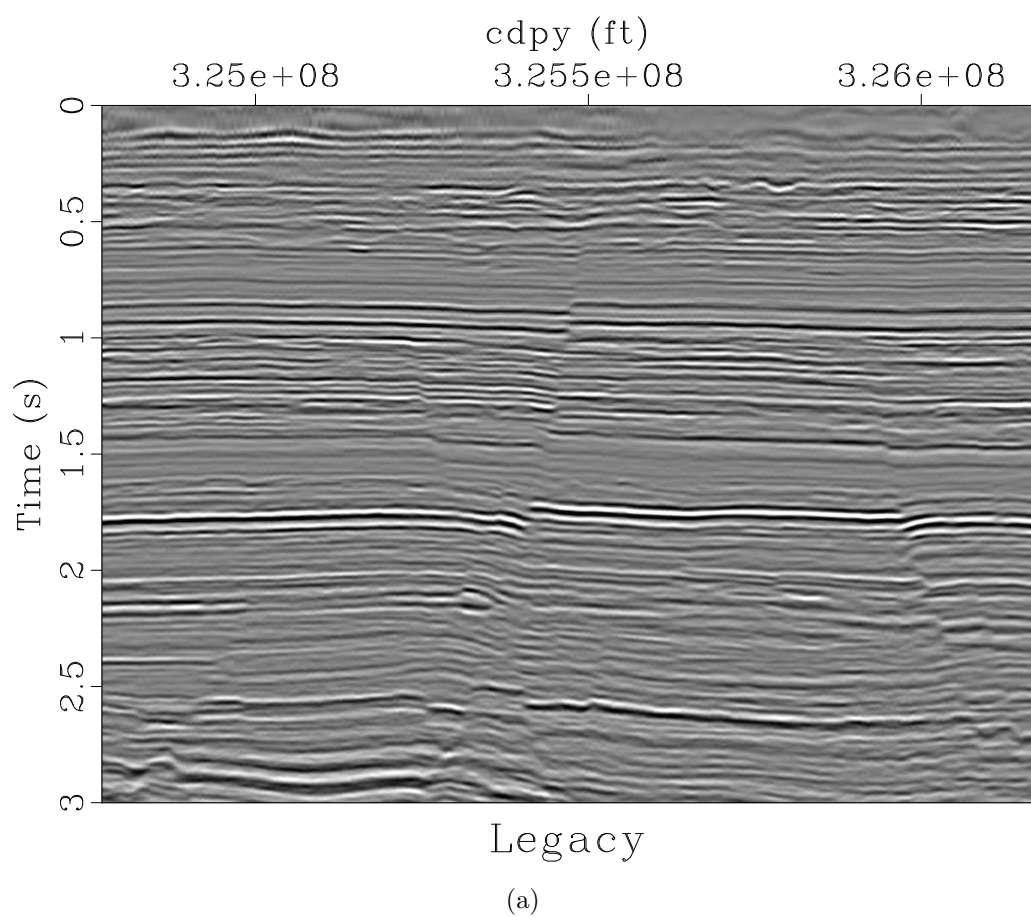
EXAMPLES

This method is applicable to workflows that require matching data with different frequency content. In this paper, we demonstrate two examples where smoothing data before matching produces better results.

Matching legacy and high-resolution images

High-resolution seismic data, such as those acquired with the P-cable acquisition system, can produce very detailed images of the near subsurface (Meckel and Mulcahy, 2016). When compared to conventional seismic images, high-resolution images have a higher dominant frequency and a larger frequency bandwidth. However, they usually lack low frequency content and depth coverage that is present in conventional seismic images. As a result, successful interpretation of high-resolution images can be aided by matching with legacy data coverage over the same area.

Example legacy and high-resolution images of the same subsurface are shown in Figure 2.1. The first step in matching the two images is to ensure that they both have a similar frequency bandwidth so they are directly comparable. The average frequency spectra for the two images are shown in Figure 2.3(a). From this, it is evident that there is almost no overlap in frequency bandwidth between the two images. To address this problem, we apply a low-cut filter to the legacy image to remove some of the lower frequencies that are simply not present in the high-resolution image. Next, we implement the method described in the previous section to balance



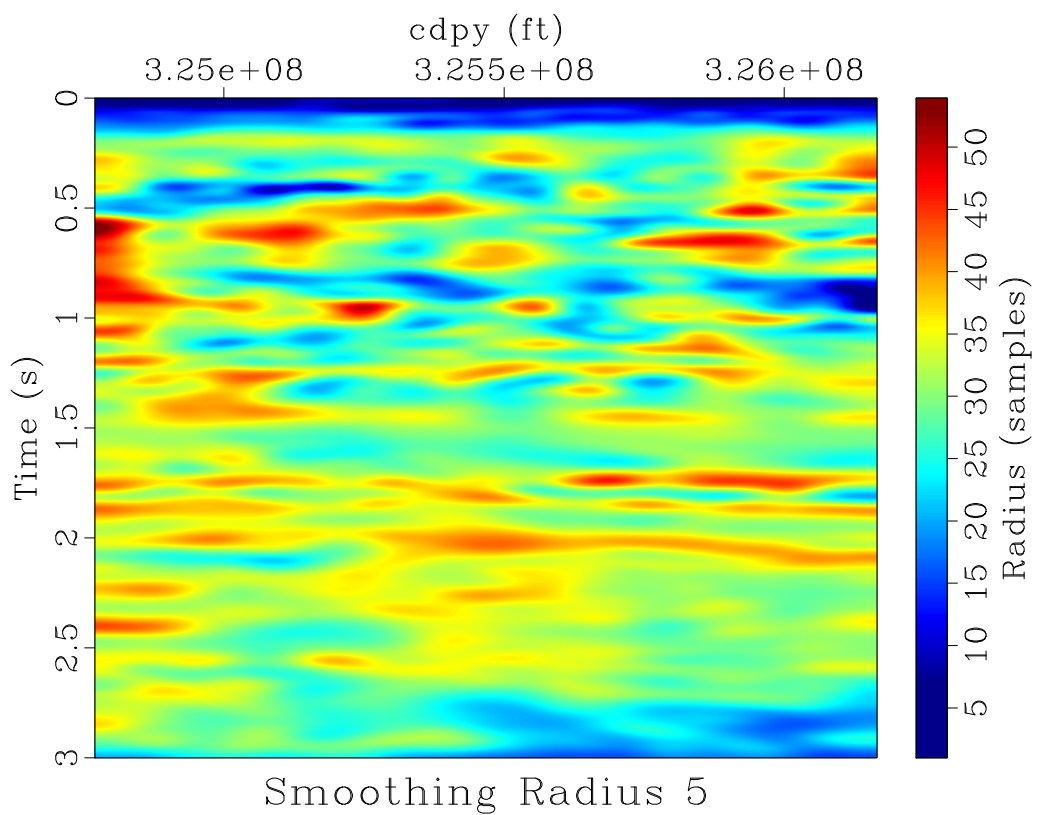


Figure 2.2: The smoothing radius, which is a function of time and space, this method produces after 5 iterations. This represents the number of samples in time that the high-resolution image needs to be smoothed over in a triangle weight to balance local frequency content with the legacy image. `chapter-locfreq/merge rect5`

local frequency content between the two images. The difference in local frequencies (residual, by equation 3.11) between the high-resolution and legacy images before balancing frequency content and after 5 iterations of the algorithm in equation (4.2) is shown in Figure 2.4. After balancing local frequencies, the images show a similar spectral bandwidth (Figure 2.3(b)), which helps increase the correlation between the two images and makes matching reflections better defined.

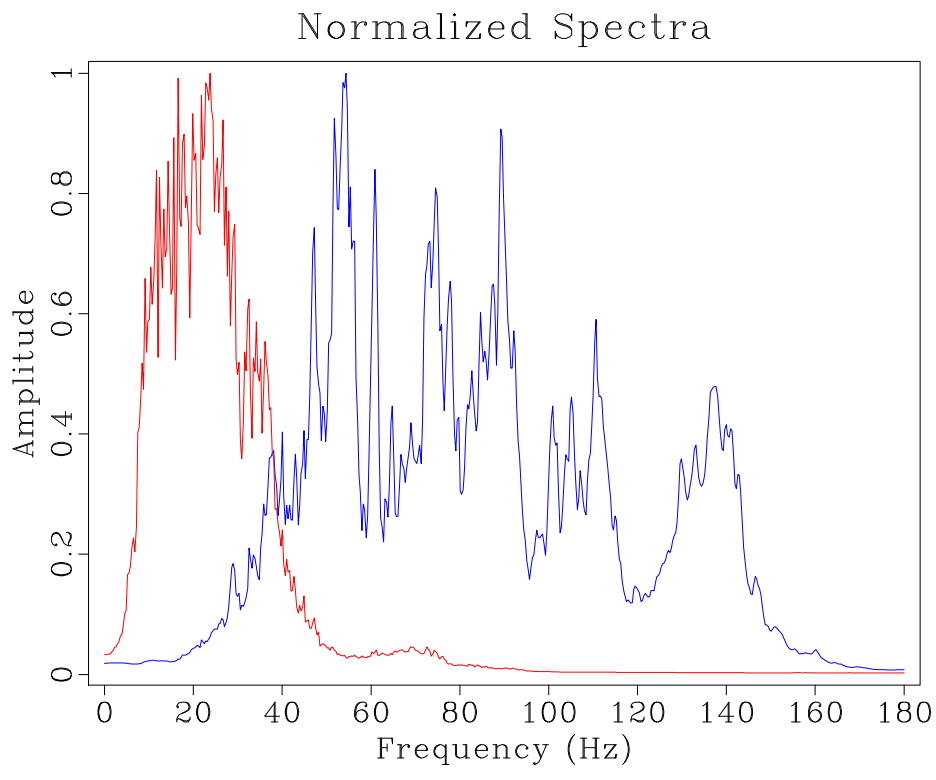
After the frequency content is matched, the optimal time shift is found to align signal content between the legacy and high-resolution images. We then apply this time shift to the original high-resolution image—the frequency content is only degraded for the purpose of finding the time shift.

An application of aligning the high-resolution and legacy images is discussed in the companion paper (Fomel, 2018).

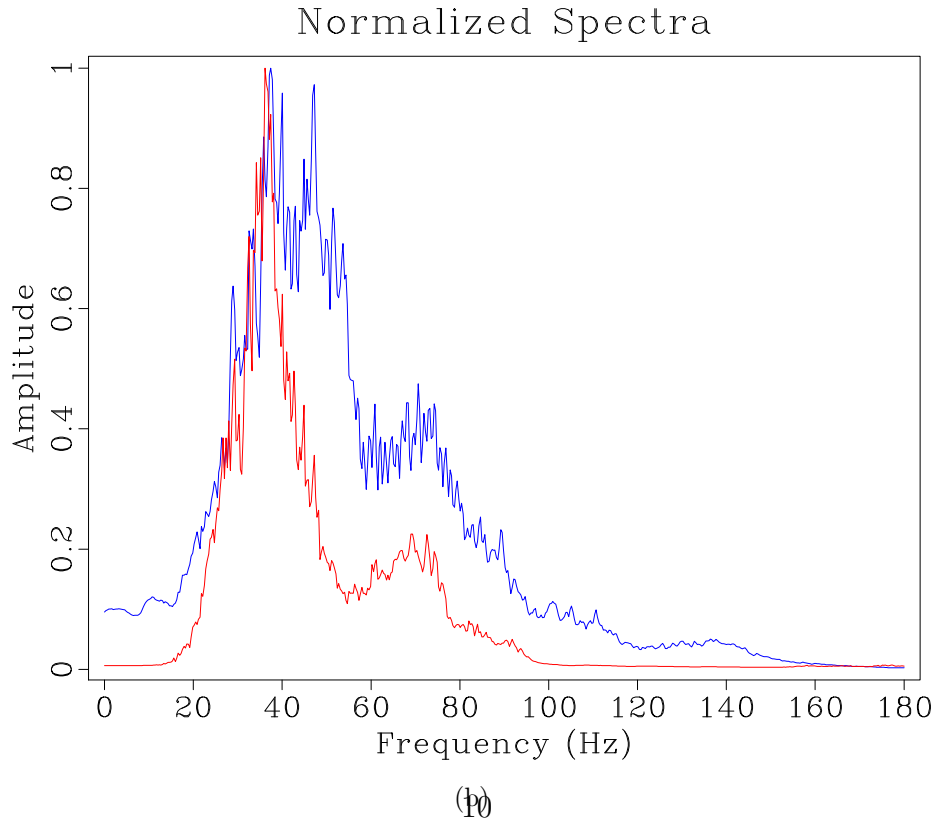
Multicomponent image registration

Multicomponent seismic image registration is an important step before the interpretation of P and S images of the subsurface. It involves warping the space of S images to align reflections with the analogous reflections of P images (Fomel and Backus, 2003a; Fomel et al., 2005).

Figure 2.5 shows PP and SS images from a 9-component seismic survey (Fomel, 2007a). To properly register the images, we follow the method proposed in Fomel et al. (2005). It consists of three primary steps: (1) initial registration of PP and SS images using initial interpretation and well-log analysis; (2) balancing frequency and amplitude content; and (3) final registration using residual local similarity scanning. We incorporate our method of balancing frequency content into the second step in



(a)



(b)

Figure 2.3: Spectral content of the legacy (red) and high-resolution (blue) images before (a) and after (b) spectral balancing.
 chapter-locfreq/merge nspectra-orig,high-smooth-spec5

this process.

Before initial registration, the PP image has much higher frequency content than the SS image. After the SS image is temporally compressed to PP time for initial registration, the two images have more similar frequency content. However, additional frequency balancing is still needed before residual registration. This poses a problem as neither image has distinctly higher frequencies than the other, so both images need to be smoothed in different areas to balance frequency content. In order to do this, we modify the proposed method to include two separate smoothing operators—one for each image.

We modify the objective in equation (2.1) as

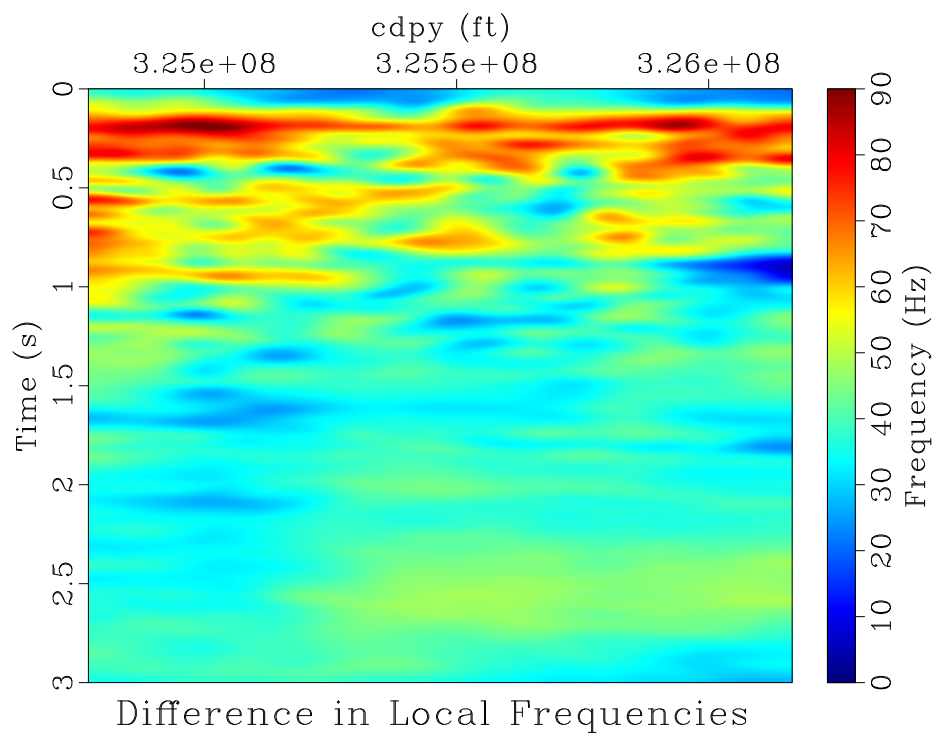
$$\min_{\mathbf{R} \in [-N, -1] \cup [1, N]} \left\| \mathbf{F}[\mathbf{S}_{\mathbf{R}_p} \mathbf{d}_p] - \mathbf{F}[\mathbf{S}_{\mathbf{R}_s} \mathbf{d}_s] \right\|, \quad (2.4)$$

where \mathbf{d}_p and \mathbf{d}_s are the PP and SS images, respectively, and $\mathbf{S}_{\mathbf{R}_p}$ and $\mathbf{S}_{\mathbf{R}_s}$ are the non-stationary smoothing operators for the PP and SS images, respectively. We also modify the residual from equation (3.11) as

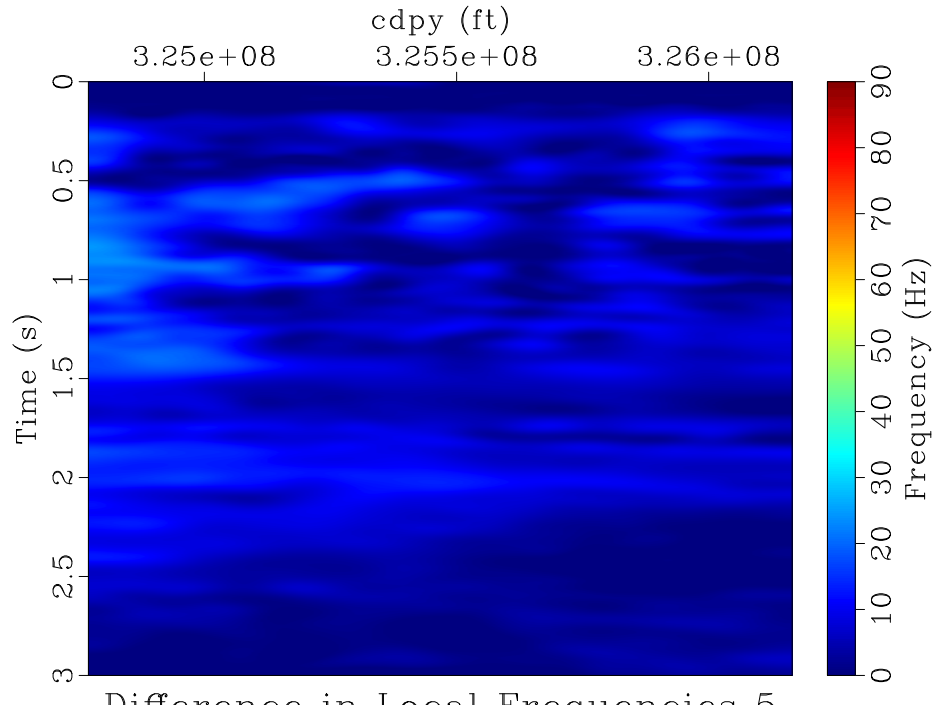
$$\mathbf{r} = \mathbf{F}[\mathbf{S}_{\mathbf{R}_p} \mathbf{d}_p] - \mathbf{F}[\mathbf{S}_{\mathbf{R}_s} \mathbf{d}_s]. \quad (2.5)$$

The ideal radius is still found using the same line-search from equation (4.2), except we allow the smoothing radius to be negative. Physically, a negative smoothing radius would signify that the image should be sharpened at that particular point instead of smoothed. In this case, instead of trying to sharpen the PP image at that particular point, we choose to smooth the SS image by the negative part of the smoothing radius. Thus, we define the i th components of \mathbf{R}_p and \mathbf{R}_s as

$$R_{p,i} = \begin{cases} R_i & \text{if } R_i \geq 1 \\ 1 & \text{otherwise} \end{cases} \quad (2.6)$$



(a)



(b)

Figure 2.4: Difference in local frequencies (residual) between the legacy and high-resolution images before (a) and after (b) the 5th iteration of frequency balancing.

`chapter-locfreq/merge freqdif,freqdif-filt5`

and

$$R_{s,i} = \begin{cases} |R_i| & \text{if } R_i \leq -1 \\ 1 & \text{otherwise} \end{cases} \quad (2.7)$$

where R_i is the i th component of \mathbf{R} and a radius of 1 represents no smoothing.

This allows each image to be smoothed in different areas to balance the frequency content between the two images.

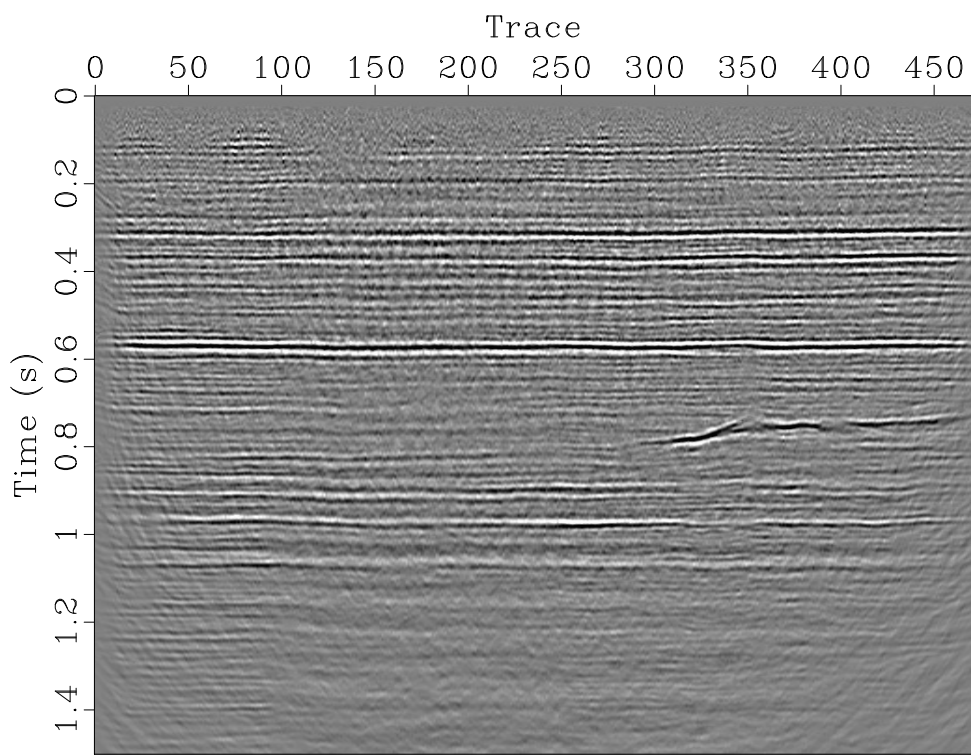
The results of using this spectral balancing method are shown in Figure 2.6. Comparable results were achieved in Liu and Fomel (2012), who used LTFD to balance the spectral content between the two images. However, the method we propose in this paper is more straightforward and significantly less computationally expensive.

CONCLUSIONS

It is difficult to compare signals with differing frequency content because signals with differing frequencies are hard to correlate. In this paper, we proposed a method of balancing frequency content between data which takes the form of an optimization problem solved by a simple iterative algorithm. It is a relatively inexpensive and effective method compared to previously proposed methods of balancing frequencies between data sets. We applied this method to examples of matching seismic images of differing resolution and for multicomponent image registration.

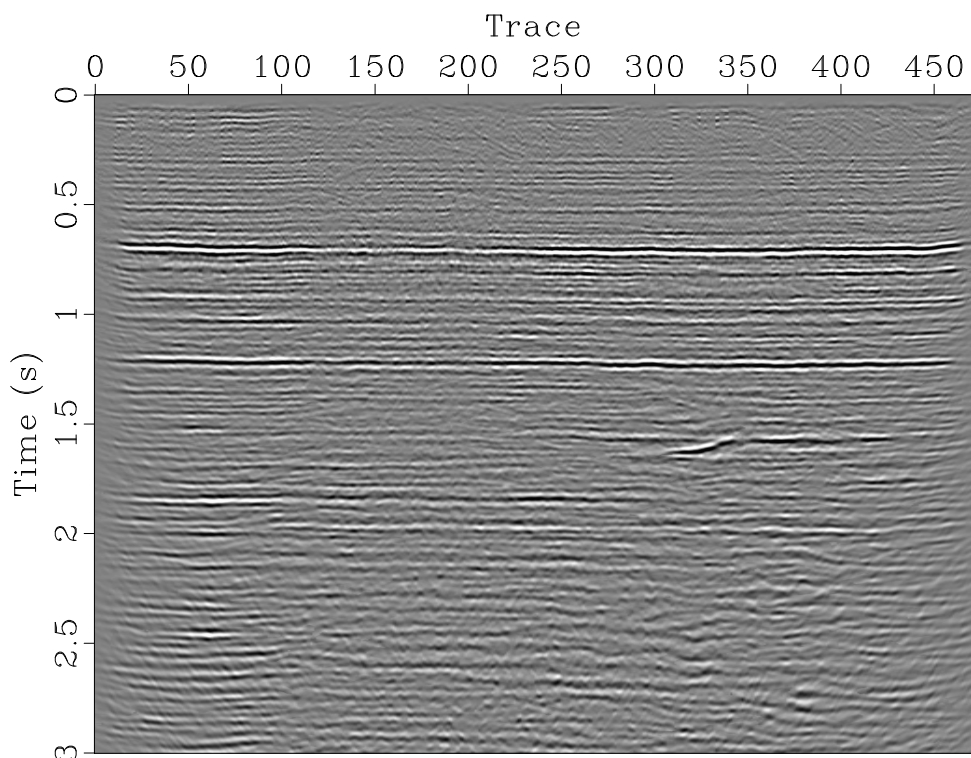
ACKNOWLEDGEMENTS

We thank the sponsors of the Texas Consortium for Computational Seismology (TCCS) for their financial support.



PP

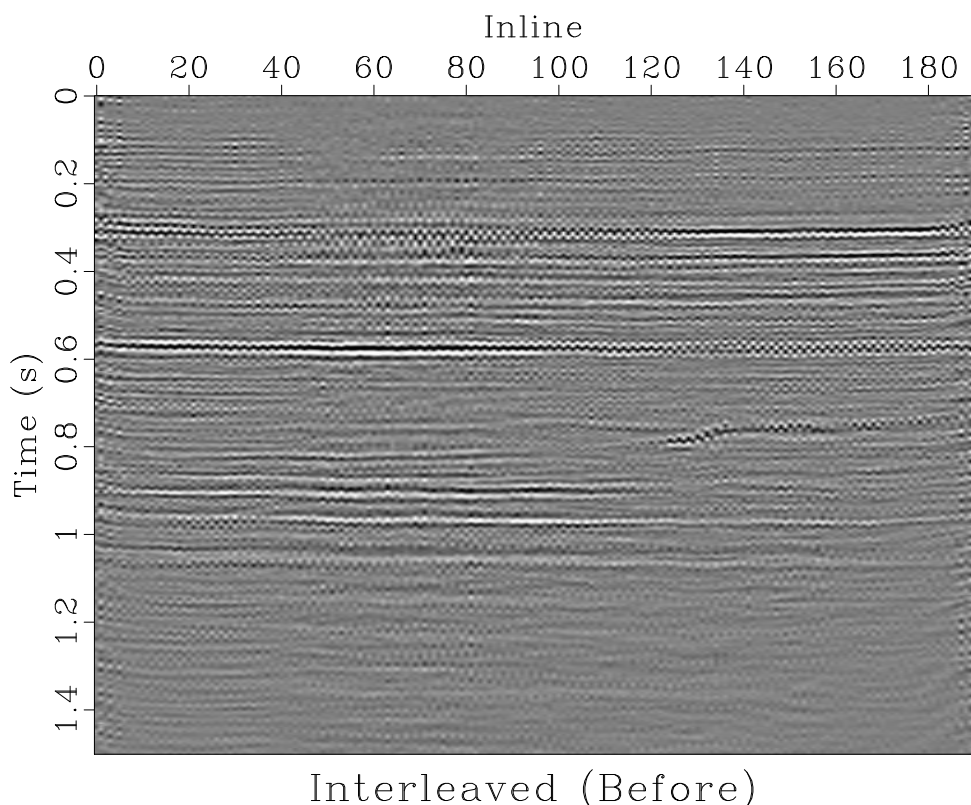
(a)



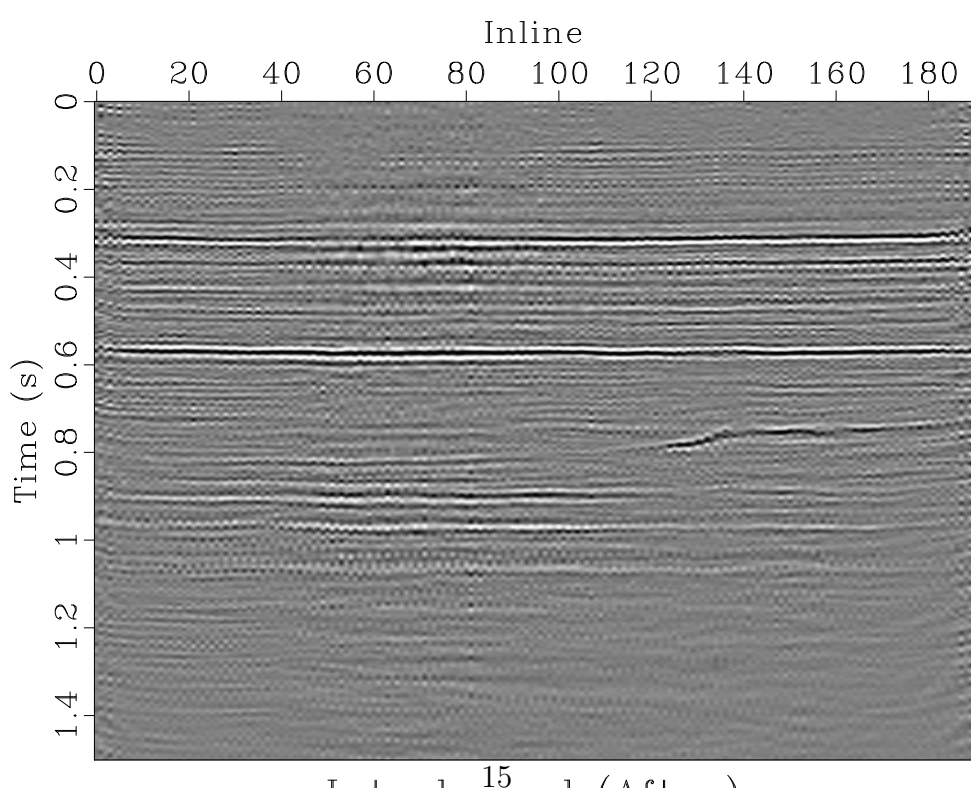
14SS

(b)

Figure 2.5: Initial PP (a) and SS (b) images. chapter-locfreq/vecta pp,ss



(a)



(b)

Figure 2.6: Interleaved PP and warped SS traces before (a) and after (b) frequency balancing and residual registration. After registration, the signal content between the two initial images is more aligned; for example, the reflections around 0.3 and 0.6 s.

Chapter 3

Matching and merging high-resolution and legacy seismic images

When multiple seismic surveys are acquired over the same area using different technologies that produce data with different frequency content, it may be beneficial to combine these data to produce a broader bandwidth volume. We have developed a workflow for matching and blending seismic images obtained from shallow high-resolution seismic surveys and conventional surveys conducted over the same area. The workflow consists of three distinct steps: (1) balancing the amplitudes and frequency content of the two images by non-stationary smoothing of the high-resolution image, (2) estimating and removing variable time shifts between the two images, and (3) blending the two images together by least-squares inversion. Our workflow is applied successfully to images from the Gulf of Mexico.

INTRODUCTION

Modern high-resolution seismic acquisition systems, such as P-cable (Petersen et al., 2010; Meckel and Mulcahy, 2016), can produce detailed images of the subsurface at shallow depths. These images often need to be compared with those previously produced using legacy images from conventional seismic acquisition. In comparison with high-resolution images, conventional images have generally lower frequency content and correspondingly lower resolution, but better signal content at greater depth. To

reconcile the differences between the two types of images, they need to be properly matched.

Analogous problems occur when interpreting images from multicomponent seismic acquisition. In particular, single-component PP and converted PS images often exhibit significantly different frequency content and need to be balanced for accurate registration (Hardage et al., 2011; Fomel and Backus, 2003b; Fomel et al., 2005).

When multiple data sets are acquired over the same area using different technologies, it is likely that these data sets contain signal content from different frequency bands, which correspondingly contain unique information about the subsurface. In order to utilize all available information, it may be beneficial to produce a consolidated broad-bandwidth volume that combines these data sets. Many previous methods of seismic data merging have been developed for the purpose of increasing the spatial coverage of the merged volume by combining data from partially overlapping areas. This usually involves steps such as rebinning for data alignment, along with spectral and phase matching. As a result, both the initial and resultant merged images poses similar signal characteristics, most notably spectral content (Mohan et al., 2007; Zhou et al., 2014; Al-Inaizi et al., 2004). However, previously Carter and Pambayuning (2009) are successful in applying a frequency domain merge to two separate seismic volumes over the same area to broaden the effective bandwidth.

In this paper, we consider the problem of matching seismic images obtained in the same area with different resolution. Using techniques borrowed from multicomponent image processing (Fomel et al., 2005), we propose a multistep approach. First, we balance the two images in amplitude and frequency content. As a result, the

resolution of the high-resolution image is temporarily degraded to match the resolution of the legacy data. Next, we measure shifts between images using local similarity scanning (Fomel, 2007a; Fomel and Jin, 2009). Finally, when the images are aligned and matched, we create a blended image using least-squares inversion in the time domain. The blended image has a wider frequency bandwidth than the two initial images, along with coherent signal content with depth from the legacy image and detailed shallow coverage from the high-resolution image.

We test the proposed approach using data from the Gulf of Mexico. A 2D image is used to illustrate the method, followed by an example applied to 3D data.

METHOD

The initial legacy and high-resolution example images are shown in Figure 3.1. They both underwent standard marine processing flows, and are assumed to be optimally processed. The images show similar structures, particularly at shallow depths, but with strikingly different resolution. The main difference comes from the broader frequency bandwidth of the high-resolution image in comparison with that of the legacy image. Therefore, our first step in comparing the two images is balancing their spectral content.

Balancing spectral content

Analyzing the spectra of the legacy and high-resolution images, as seen in Figure 3.2(a), it is clear that the high-resolution image has a wider range of frequencies with a higher dominant frequency than the legacy image. In order to match these images, our first step is to balance their spectral content. We can achieve this by

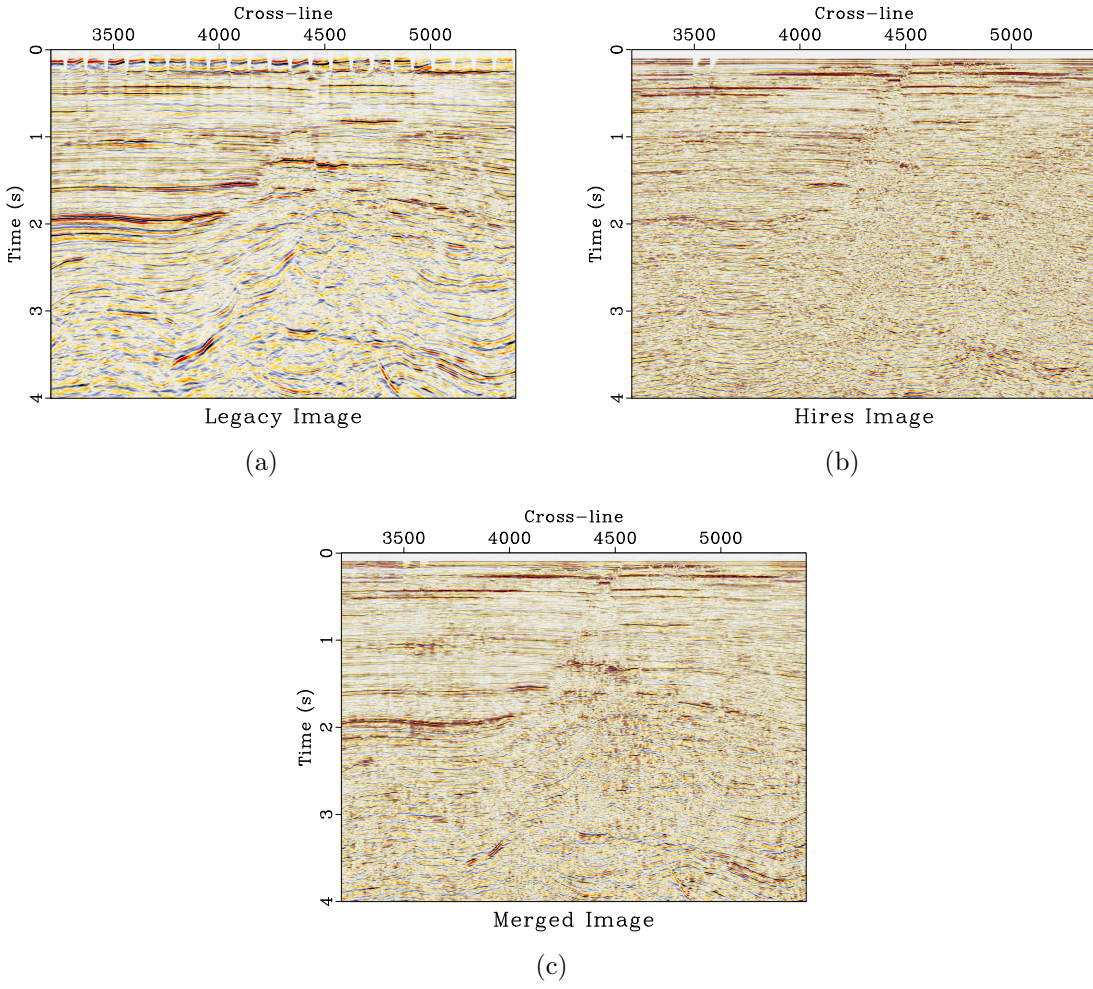
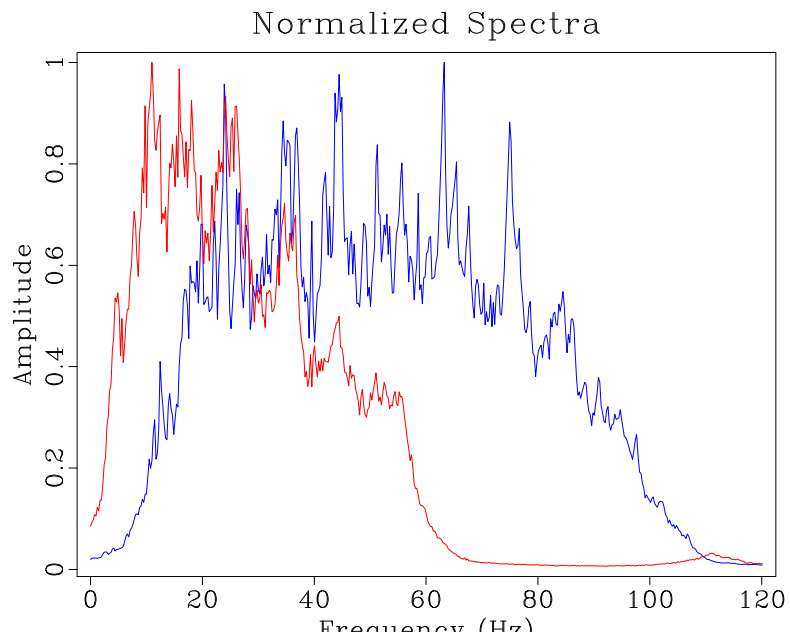


Figure 3.1: The initial legacy (a) and high-resolution (b) images. The merged image (c) is the final product of the proposed workflow: the combination of both the legacy and high-resolution images. chapter-merge/apache legacy,hires,merge2-reverse

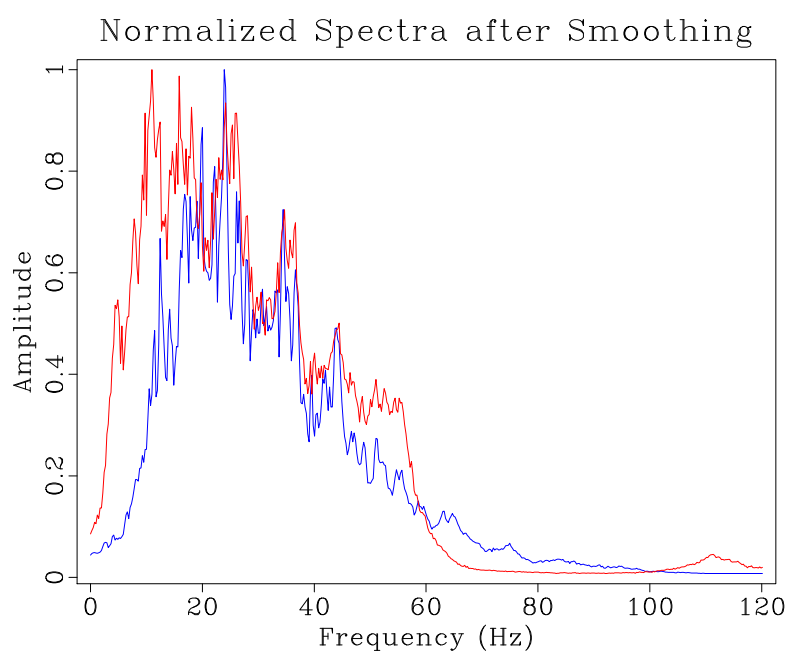
attenuating the high frequencies of the high-resolution image to match the lower frequency content of the legacy image. One approach to frequency balancing is to apply a stationary bandpass filter to the high-resolution image. However, this does not take into account local frequency variations in each image caused by seismic wave attenuation. A more effective method, which accounts for temporally and spatially variable frequency content that is present in most seismic data, is to apply a non-stationary filter using frequency information from both images. To accomplish this, we use a simple triangle smoothing operator with an adjustable radius. Here, the radius at each point is the amount of time, in seconds, that that specific data point gets averaged over in a triangle weight in the temporal direction. We specifically look at local frequency (Fomel, 2007a), which is a time-dependent frequency attribute, and can be thought of as a smoothed estimate of instantaneous frequency (White, 1991). For the procedure described in this paper, local frequency is a better-suited attribute than instantaneous frequency. Local frequency allows the comparison of frequency content in a local region of samples, as opposed to instantaneous frequency, which allows for a point by point comparison of frequency values between images. Because the corresponding reflections between images may not be precisely aligned in time at this stage in the method, using the local frequency attribute to balance frequency content between images would allow for more accurate frequency balancing than instantaneous frequency.

The justification for triangle smoothing is that it is a simple approximation to Gaussian smoothing. The frequency response of the triangle smoothing filter (Claerbout, 1992) is

$$T(f) = \text{sinc}^2\left(\frac{2\pi f \Delta t}{2}\right) \approx 1 - \frac{(2\pi f)^2 (\Delta t)^2}{12}. \quad (3.1)$$



(a)



(b)

Figure 3.2: Spectra for the entire image display of the legacy (red) and high-resolution (blue) images before (a) and after (b) spectral balancing.

`chapter-merge/apache nspectra,hires-smooth-spec`

This frequency response resembles that of a Gaussian:

$$G(f) = e^{-\alpha f^2} \approx 1 - \alpha f^2 . \quad (3.2)$$

If the signals' spectra can be represented by Ricker wavelets,

$$S_n(f) = A_n \left(\frac{f}{f_n} \right)^2 e^{-\left(\frac{f}{f_n}\right)^2} \quad (3.3)$$

where, in image n , S_n is the frequency spectrum, f_n is the peak frequency, and A_n is the amplitude, Gaussian smoothing can transform the signal to a different dominant frequency.

Because we are smoothing the high-resolution image to match it with the legacy image, we can relate the high-resolution frequencies, S_h , to the legacy frequencies, S_l , such that

$$S_l(f) = A e^{-\alpha f^2} S_h(f) \quad (3.4)$$

where $A = A_l/A_h$,

$$\alpha = \frac{1}{f_l^2} - \frac{1}{f_h^2} , \quad (3.5)$$

and the subscripts l and h correspond to the legacy and high-resolution images, respectively.

Combining equations (3.1), (3.2), and (3.5) leads to the specification of the triangle smoothing radius as

$$\Delta t \approx \frac{1}{2\pi} \sqrt{12 \left(\frac{1}{f_l^2} - \frac{1}{f_h^2} \right)} . \quad (3.6)$$

Here, Δt is the radius of smoothing, measured in seconds, applied to the high-resolution image to match the frequency content with the legacy image at each sample. The calculated smoothing radius for this data set is shown in Figure 3.3.

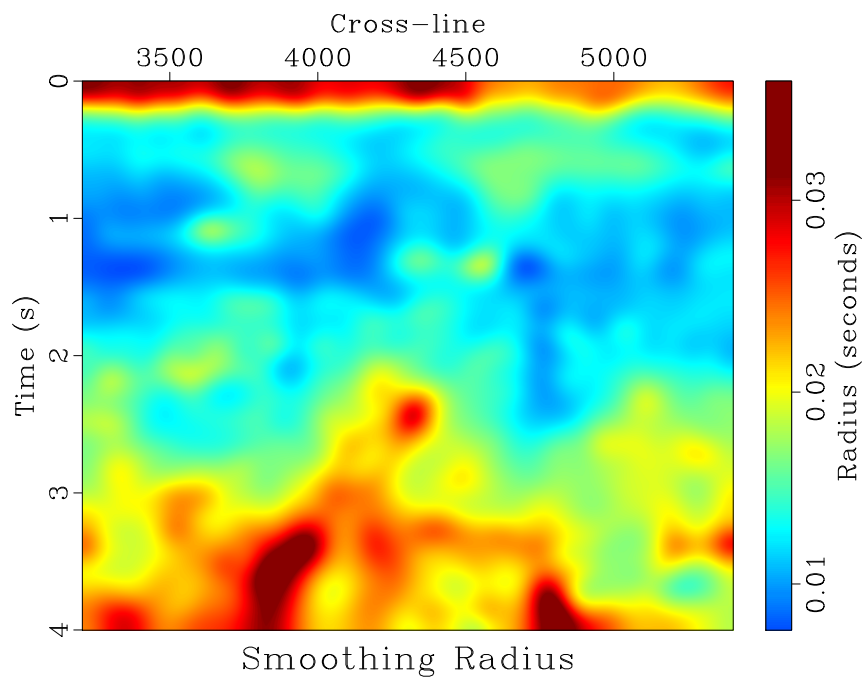


Figure 3.3: Calculated spatially and temporally variable smoothing radius. This represents the number of seconds in the temporal direction that the high-resolution image gets averaged over in a triangle weight to balance local frequency content with the legacy image at each sample. chapter-merge/apache rect

We measure local frequencies in both images and apply smoothing specified by equation (3.6) to the high-resolution image. Since this is only an approximation of what the smoothing radius should be under ideal conditions, we adjust the constant 12 in the equation to achieve a better match. In this example, this effectively reduces the difference between the spectral content of the images, as shown in Figure 3.2(b). Figure 3.4 shows the difference in local frequencies before and after smoothing. After smoothing, the frequency difference is minimized.

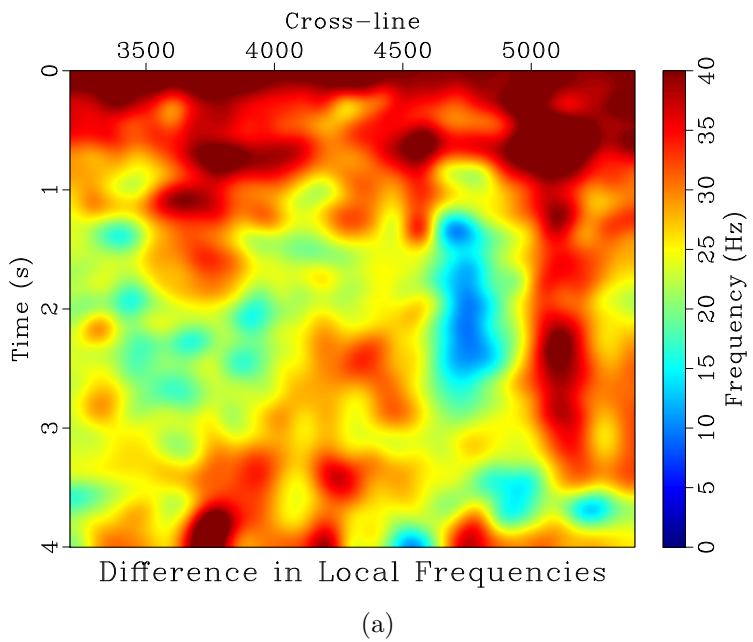
This method works well for simple data sets with overlapping frequency content. However, more complicated data sets, as seen in the next example, may require additional steps for successful frequency balancing.

In addition to frequency balancing, we initially attempted accounting for wavelet phase differences between data sets at this step. However, we saw this had a negligible impact on the final result, so we decided not to include it in this method.

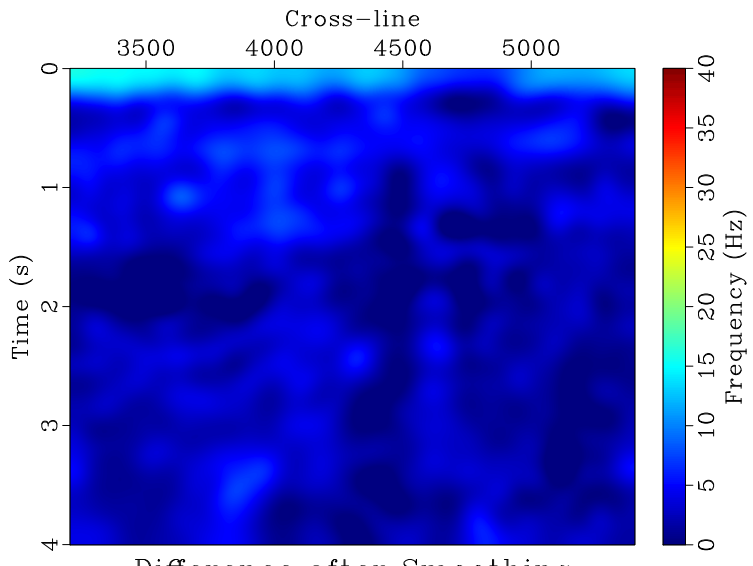
Measuring time shifts

After balancing the spectral content, we attempt to account for possible time shifts of the high-resolution image relative to the legacy image, which can be caused by changes in acquisition and processing parameters. We measure this shift using local similarity scanning (Fomel, 2007a; Fomel and Jin, 2009). In this method, we detect the relative time shift by first calculating the local similarity at different time shifts of the high-resolution image relative to the legacy image (Fomel and Jin, 2009). From this, the trend of the highest similarity is picked and represents the relative time shift between the two images.

Next, we apply the estimated time shift to the original high-resolution image—



(a)



(b)

Figure 3.4: Difference in local frequencies between the legacy and high-resolution images before (a) and after (b) balancing their frequency content by non-stationary smoothing. chapter-merge/apache freqdif,freqdif-filt

the frequency content is only degraded for the purpose of finding the time shift that best aligns the signal content between the two images. The differences between the two images before and after the time shift correction are shown in Figure 3.5, and demonstrate a noticeably better match resulting from the time shift. Similar results were achieved using amplitude-adjusted plane-wave destruction, which involves balancing amplitudes and temporally aligning the data sets simultaneously (Phillips and Fomel, 2016).

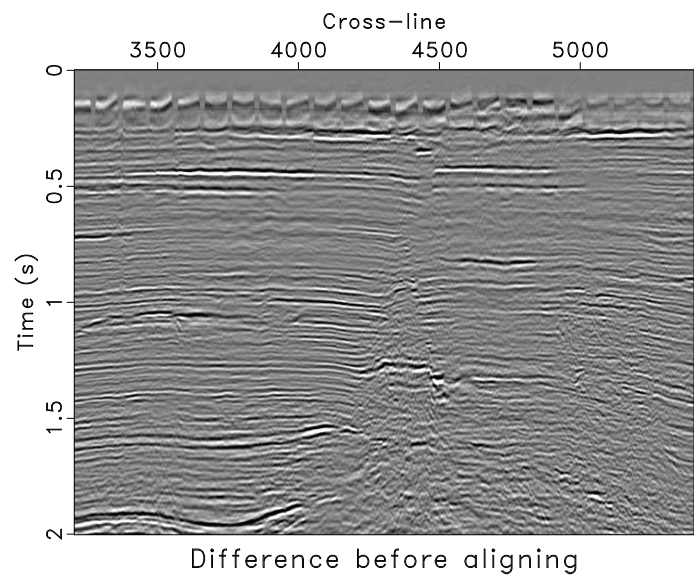
Creating the blended image

Since the high-resolution and legacy images contain information about the same subsurface, we can attempt to create an optimal image of this area by blending the two images together to combine the strengths of each while minimizing their weaknesses. We can achieve this by imposing two conditions. First, the blended image should match the high-resolution image, particularly in the shallow part. Second, after smoothing with the non-stationary smoothing operator, the blended image should match the legacy image. We combine the two conditions together in the least-squares system

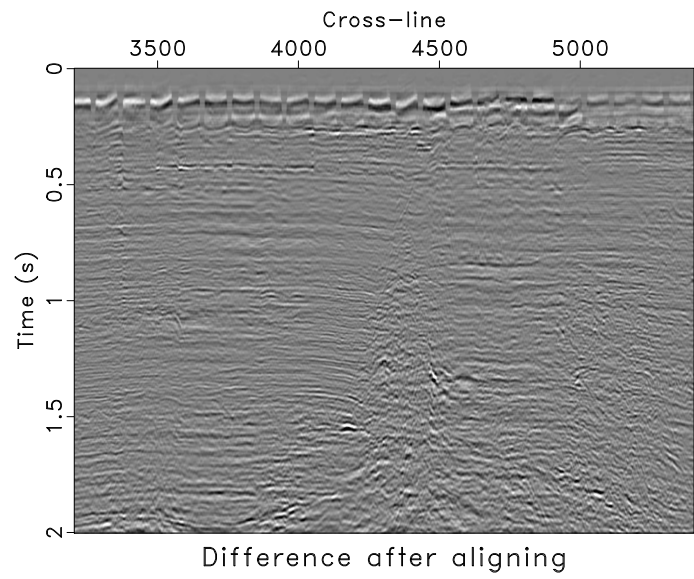
$$\begin{bmatrix} \mathbf{W}_h \\ \mathbf{W}_l \mathbf{S} \end{bmatrix} \mathbf{b} \approx \begin{bmatrix} \mathbf{W}_h \mathbf{h} \\ \mathbf{l} \end{bmatrix}, \quad (3.7)$$

where \mathbf{h} denotes the high-resolution image, \mathbf{l} is the legacy image, \mathbf{b} is the desired blended image, \mathbf{W}_h and \mathbf{W}_l are the diagonal weighting matrices for the high-resolution and legacy images, respectively, and \mathbf{S} is the non-stationary smoothing specified by equation (3.6). The formal solution of the least-squares problem (4.2) is

$$\mathbf{b} = (\mathbf{W}_h^2 + \mathbf{S}^T \mathbf{W}_l^2 \mathbf{S})^{-1} (\mathbf{W}_h^2 \mathbf{h} + \mathbf{S}^T \mathbf{W}_l \mathbf{l}). \quad (3.8)$$



(a)



(b)

Figure 3.5: Difference between the legacy and smoothed high-resolution images before (a) and after (b) aligning the data sets. Before accounting for time shifts, much of the signal content did not align in time, so coherent reflections were subtracted out. After accounting for time shifts, the reflections are more aligned, so much of the subtracted information is noise.

Alternatively, equation (3.8) can be rearranged as

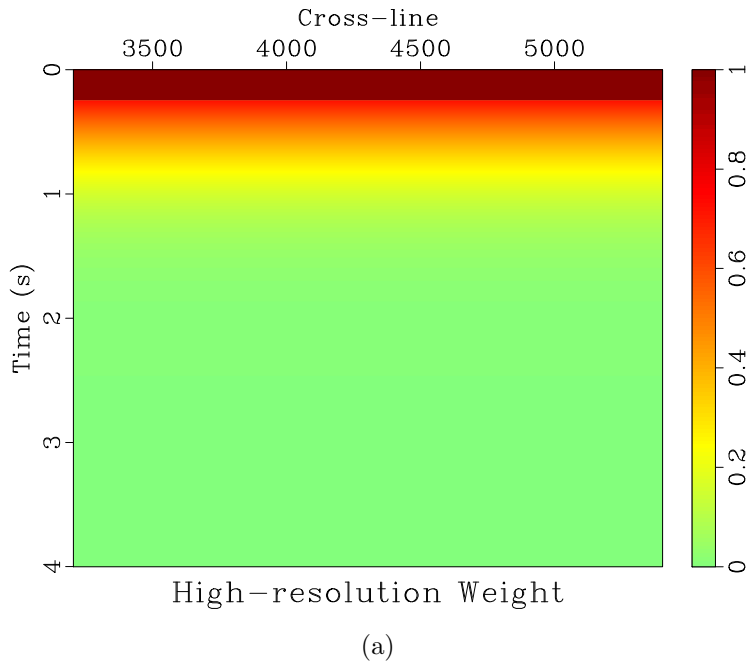
$$\begin{aligned}
\mathbf{b} &= (\mathbf{W}_h^2 + \mathbf{S}^T \mathbf{W}_l^2 \mathbf{S})^{-1} (\mathbf{W}_h^2 \mathbf{h} + \mathbf{S}^T \mathbf{W}_l^2 \mathbf{S} \mathbf{h} - \mathbf{S}^T \mathbf{W}_l^2 \mathbf{S} \mathbf{h} + \mathbf{S}^T \mathbf{W}_l \mathbf{l}) \\
&= (\mathbf{W}_h^2 + \mathbf{S}^T \mathbf{W}_l^2 \mathbf{S})^{-1} ((\mathbf{W}_h^2 + \mathbf{S}^T \mathbf{W}_l^2 \mathbf{S}) \mathbf{h} + \mathbf{S}^T \mathbf{W}_l (\mathbf{l} - \mathbf{W}_l \mathbf{S} \mathbf{h})) \\
&= \mathbf{h} + (\mathbf{W}_h^2 + \mathbf{S}^T \mathbf{W}_l^2 \mathbf{S})^{-1} \mathbf{S}^T \mathbf{W}_l (\mathbf{l} - \mathbf{W}_l \mathbf{S} \mathbf{h}),
\end{aligned} \tag{3.9}$$

which makes it evident that the merged image is simply the high-resolution image with some changes.

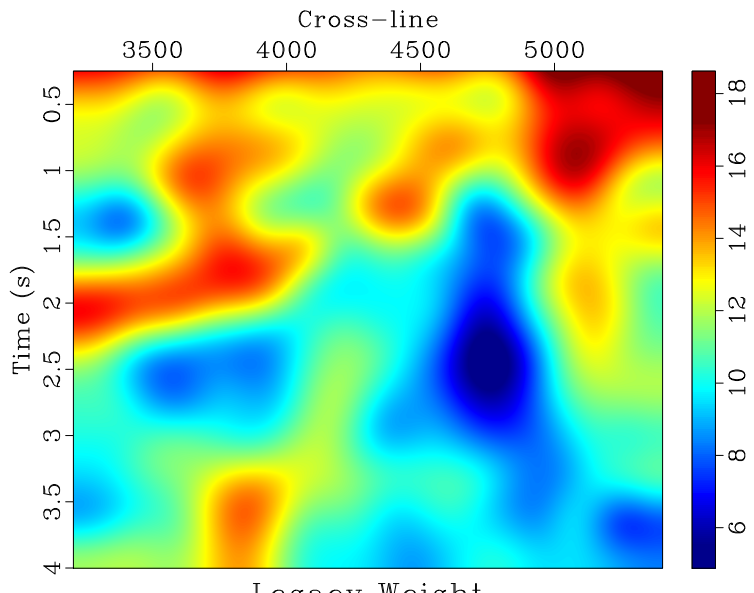
The weights, \mathbf{W}_h and \mathbf{W}_l , are applied to the images to bring out the desired qualities from each image. For example, since we prefer the high-resolution image in the shallow section, we weight it stronger there and gradually taper the weight to preference the legacy image with depth. In addition, we estimate the legacy weight, \mathbf{W}_l , to balance the legacy image's amplitudes with respect to the high-resolution image. The specific values we used for the weights are shown in Figure 3.6.

We implement the inversion in equation (3.9) iteratively using the method of conjugate gradients (Hestenes and Stiefel, 1952). The resultant blended image, shown in Figure 3.1(c), retains the higher frequencies from the high-resolution image while incorporating the lower frequencies from the legacy image (Figure 3.7). The broader frequency bandwidth corresponds to an increase in resolution and leads to a more detailed and interpretable image. As a result, the blended image resembles the high-resolution image but has a marked decrease in noise and extended coverage with depth.

Although the method presented in this paper is applied to post-stack images, the general method is likely flexible enough to be extended to pre-stack data. Applications of matching legacy and high-resolution seismic data are also seen in time-lapse



(a)



(b)

Figure 3.6: The weights for the high-resolution (a) and legacy (b) images for the least-squares merge. The high-resolution weight is strongly weighted in the shallow part and blends to favor the legacy image with depth. The legacy weight is selected to boost the legacy image's relative amplitudes to match that of the high-resolution image.

chapter-merge/apache hweight,lweight-reverse

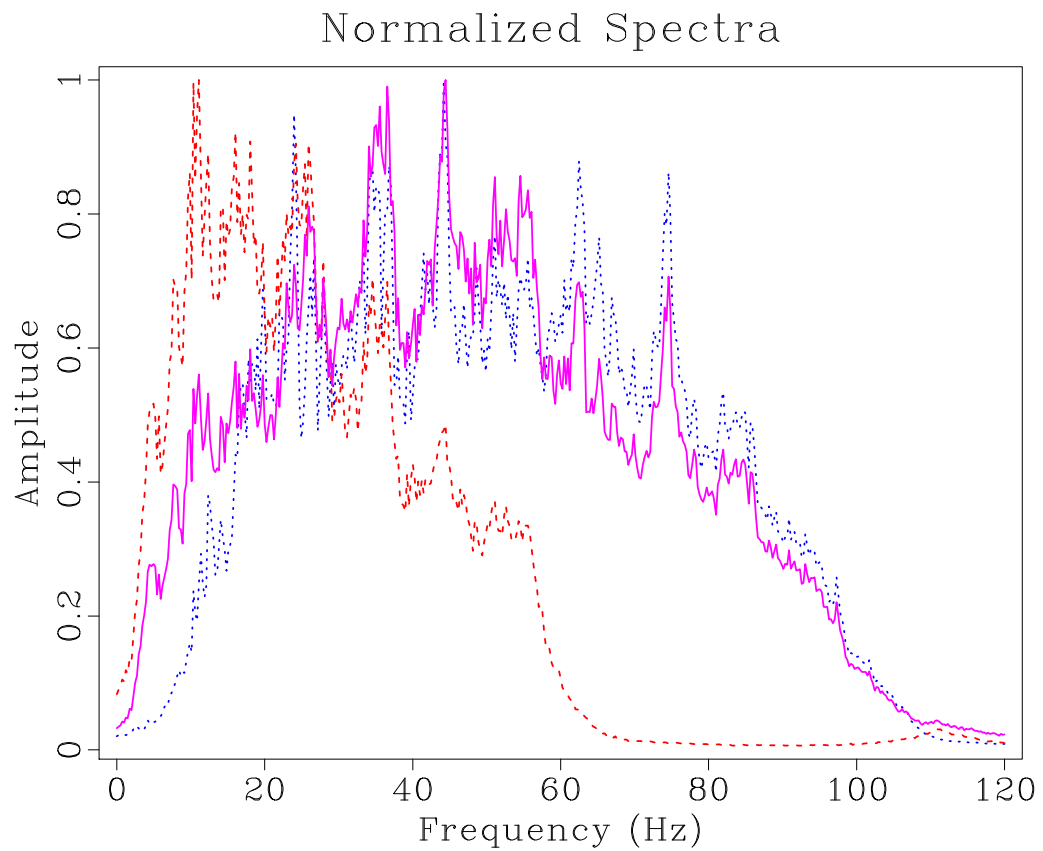


Figure 3.7: The spectra of the entire image display of the legacy (red dashed), high-resolution (blue dotted), and merged (magenta solid) images for the first data set.

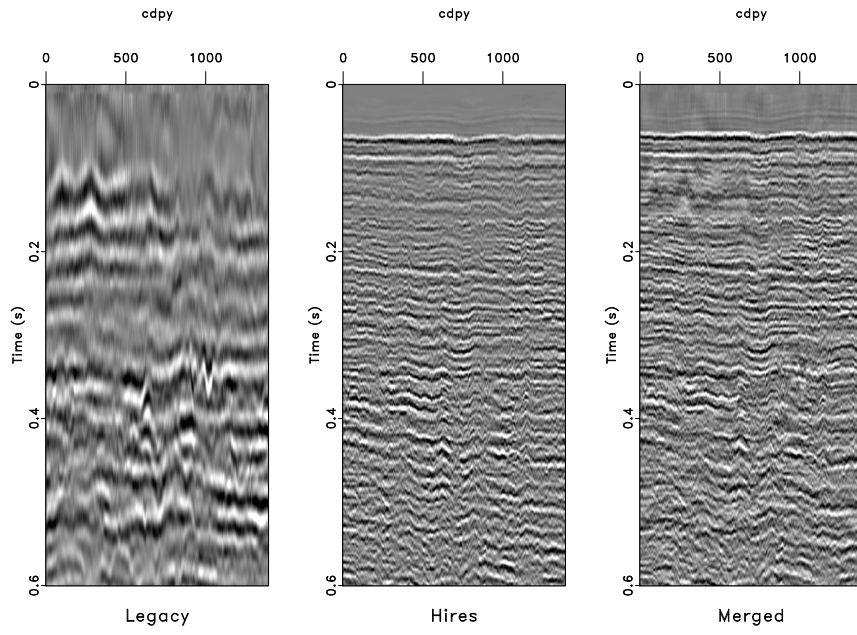
```
chapter-merge/apache nspectra22-reverse
```

image registration, where the accurate interpretation of 4D time-lapse data heavily depends on dataset alignment and uniform processing (Ross and Altan, 1997). The method from this paper could also be used in 4D time-lapse processing; particularly the steps involving frequency balancing and accounting for time shifts.

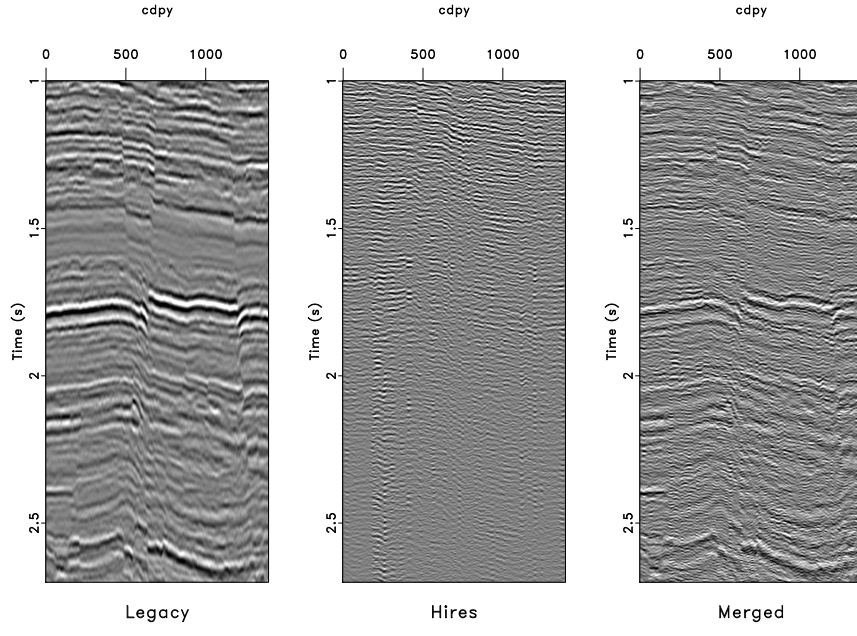
P-CABLE EXAMPLE

Our second example refers to data from the inner shelf of the Gulf of Mexico, just off of San Luis Pass, Texas (Meckel et al., 2017). The high-resolution P-cable data set was acquired from a shallow marine environment in the Gulf of Mexico. The area of interest for this survey was the near subsurface, and a high frequency source was used which allows for exceptional resolution in the shallow section, at the expense of less coherent signal information at depth caused by attenuation (Meckel and Mulcahy, 2016). In addition, very little low-frequency information is present in the P-cable data because of the high-frequency source used, which makes balancing spectral content particularly difficult. The other image comes from legacy data coverage over the same area, which has better signal continuity at depth than the high-resolution P-cable data. This is apparent by looking at the first few hundred milliseconds of data for both data sets (Figure 3.8).

Due to the nature of acquisition, the high resolution image has very dense spatial coverage, providing detailed time slices of the near subsurface (Meckel and Mulcahy, 2016). The legacy image has lower spatial resolution. As a result, when matching the high-resolution and legacy images spatially, the high spatial resolution of the high-resolution image must be degraded to match that of the legacy image. We rebinned the legacy and high-resolution images to align them spatially for comparison (Figure 3.10). We chose to spatially down-sample the high-resolution image to match



(a)



(b)

Figure 3.8: The first 600 ms of data from a sample line from the legacy, high-resolution, and merged image (a). The same images with depth for the legacy, high-resolution, and merged images (b). The merged image resembles the high-resolution image in the shallow parts and incorporates the more coherent lower frequency information from the legacy image with depth. [chapter-merge/pcable window1,window2]

the legacy image as opposed to interpolating the legacy image to the high-resolution image's spatial grid to prevent potentially introducing inaccurate data in the merged image.

There is a definite separation in frequency content when comparing the legacy and high-resolution images (Figure 3.9). Because there is not much overlap in frequency bandwidth, balancing their spectral content is challenging. In addition, a primary assumption made in deriving the theoretical smoothing radius (equation 3.6) is that the signal is modeled by a summation of Ricker wavelets, which may not be a correct assumption. As a result, additional steps must be taken beyond applying the smoothing specified by equation (3.6) to ensure matching frequency content.

We first apply a low-cut filter to the legacy data to remove the low frequency information that is simply not present in the high-resolution image. Next, we adjust the non-stationary smoothing radius using a simple iterative algorithm (Greer and Fomel, 2017).

The main premise behind the algorithm comes from the fact that, in general, the greater the smoothing radius at a specified point, the more high frequencies are attenuated by smoothing. We choose an initial guess of the non-stationary smoothing radius before applying corrections based on two primary assumptions:

1. The smoothing radius is too *small* at a specified point if, after smoothing, the high-resolution image has *higher* local frequency than the legacy image. Thus, the smoothing radius must be *increased* at that point.
2. The smoothing radius is too *large* at a specified point if, after smoothing, the high-resolution image has *lower* local frequency than the legacy image. Thus,

the smoothing radius must be *decreased* at that point.

We apply these assumptions using a line-search method:

$$\mathbf{R}^{(i+1)} = \mathbf{R}^{(i)} + \alpha \mathbf{r}^{(i)}, \quad (3.10)$$

where $\mathbf{R}^{(i)}$ is the smoothing radius at the i th iteration, α is a scalar constant that can be thought of as the step length, and $\mathbf{r}^{(i)}$ is the residual at the i th iteration, which can be thought of as the search direction, and is defined as

$$\mathbf{r} = \mathbf{F}[\mathbf{S}_\mathbf{R} \mathbf{d}_h] - \mathbf{F}[\mathbf{d}_l], \quad (3.11)$$

where $\mathbf{S}_\mathbf{R}$ is the non-stationary smoothing operator of smoothing radius \mathbf{R} , \mathbf{d}_h is the high-resolution image, \mathbf{d}_l is the legacy image, and \mathbf{F} is the local frequency operator. It can be noted that when equation (3.11) is positive, the high-resolution image still has a higher local frequency value at that specific point than the legacy image; thus the high-resolution image is under-smoothed and the smoothing radius should be increased at that point. This follows the form of the first assumption. The second assumption is used when equation (3.11) is negative. When equation (3.11) is zero, the correct radius has been found and no further corrections are made. Thus, it is justifiable to set the search direction from equation (4.2) equal to the residual.

Using this method, we can continually adjust the smoothing radius until we achieve the desired result of balancing the local frequency content between the two images. In practice, this method produces an acceptable solution in approximately 5 iterations and exhibits sublinear convergence. We smooth the high-resolution image with the radius this method produces to balance local frequency content between the two images.

After this, we use the low-cut filtered legacy and smoothed high-resolution images to find estimated time shifts we need to apply to the high-resolution image to align the reflections with the legacy image. Then, we apply this estimated time shift to the original high-resolution image and blend it with the original legacy image as specified by equations (4.2) and (3.9).

The resultant merged image is shown in Figure 3.10(c). The frequency content of the merged image is shown in Figure 3.9. Here, the merged image spans the frequency bandwidth of the two initial images, thus producing a high resolution volume including optimal signal characteristics from the two initial images.

CONCLUSIONS

We propose an approach to matching seismic images of different resolutions. Our first step is non-stationary smoothing of the high-resolution image to match the spectral content and amplitudes of the legacy image. Next, we estimate the relative time shifts using local similarity scanning. After matching the two images, we create a blended image by least-squares inversion, which effectively combines the best features of the two images: the broader frequency bandwidth of the high-resolution image with the reflection continuity and deeper coverage of the legacy image. The final result is an interpretable blended image that has higher temporal resolution than either of the two initial images. Two example applications using high-resolution and legacy seismic images from the Gulf of Mexico demonstrate the effectiveness of our method.

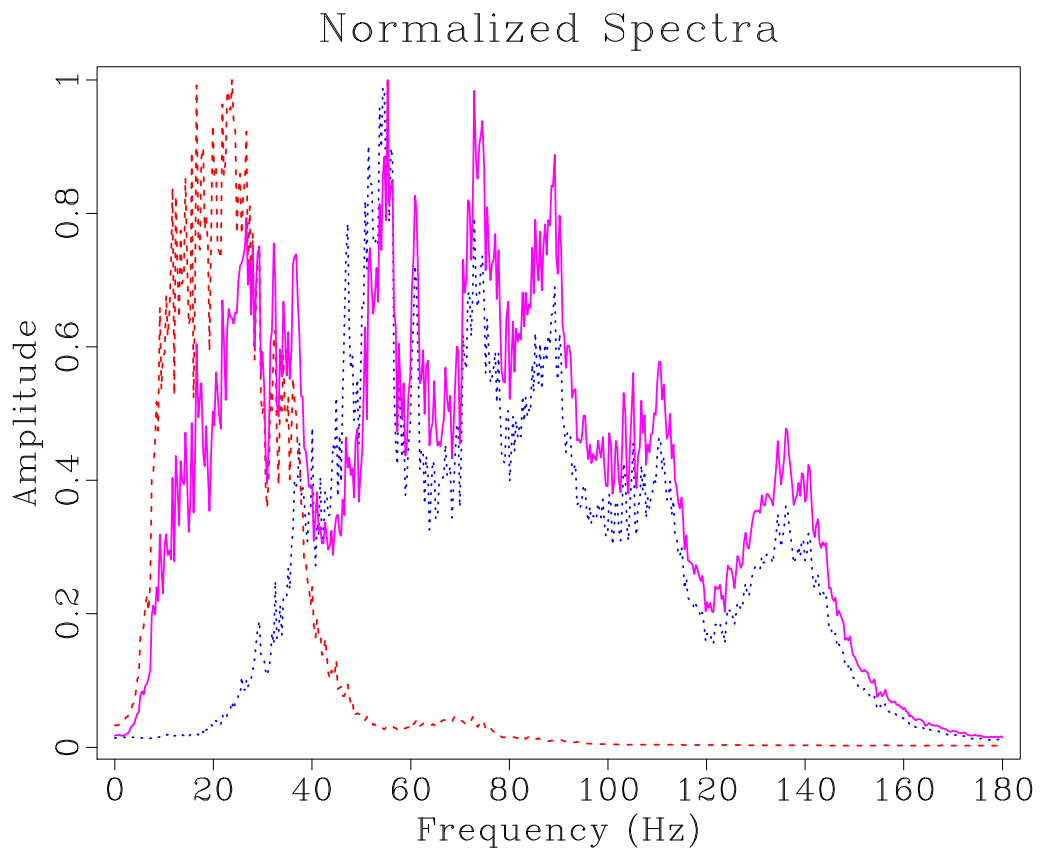


Figure 3.9: The spectral content of the entire image display of the legacy (red dashed), high-resolution (blue dotted), and resultant merged (magenta solid) images for the second data set. chapter-merge/pcable nspectra2

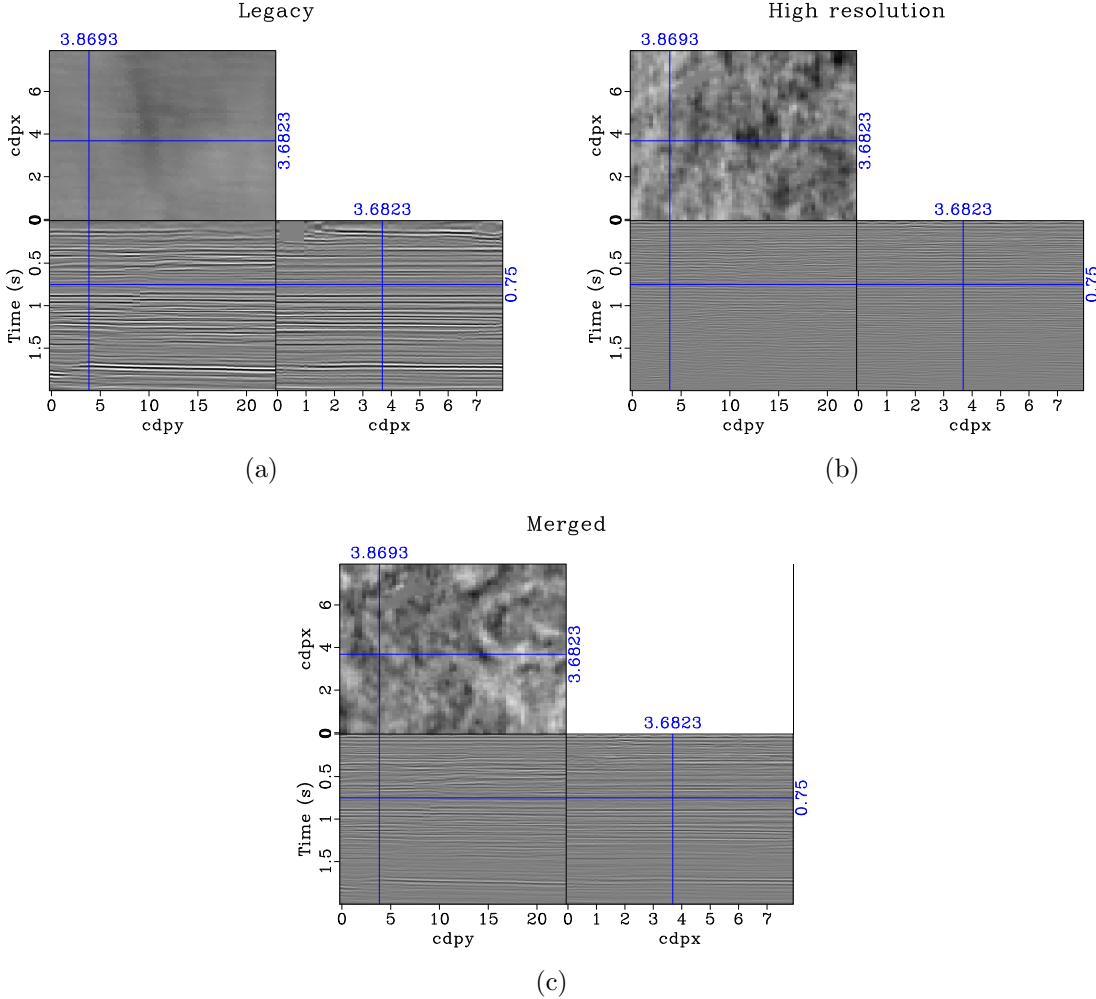


Figure 3.10: The legacy (a), high-resolution (b), and resultant merged (c) images of the second data set. chapter-merge/pcable2 legacy4,hires4,merge3

ACKNOWLEDGMENTS

We thank Michael DeAngelo, August Lau, Tip Meckel, and Chuan Yin for useful discussions and Apache and Fieldwood for providing the data used in the first example. We also thank the sponsors of the Texas Consortium for Computational Seismology (TCCS) for their financial support.

Chapter 4

Improving migration resolution by approximating the least-squares Hessian using non-stationary amplitude and frequency matching

We propose using two non-stationary operators to represent the amplitude and frequency variations in the least-squares Hessian to account for the principal differences between conventional and least-squares migrated images. The calculation and application of these operators are computationally inexpensive when compared to one iteration of least-squares migration, and it increases the resolution and amplitude fidelity of the migrated image. Successful results are achieved on an application of reverse-time migration to the Sigsbee synthetic data set.

INTRODUCTION

Least-squares migration can produce an accurate migrated seismic image. However, the process may be computationally expensive as it is typically performed in an iterative manner, where each iteration involves forward modeling and migration. Although conventional seismic migration is less computationally expensive than least-squares migration, it generally contains migration artifacts affecting amplitude fidelity and resolution (Dong et al., 2012; Dai and Schuster, 2013). This may be attributed to the fact that, while least-squares migration inverts for subsurface reflectivity by finding the least-squares model solution, standard migration amounts to applying a single adjoint operation (Claerbout, 1992).

Various methods have attempted to correct these differences by finding and applying an approximation to the inverse Hessian operator, $\mathbf{H}^{-1} = (\mathbf{L}^T \mathbf{L})^{-1}$, to a conventional migrated image. Here, \mathbf{L} is a standard forward-modeling operator, and \mathbf{L}^T is its adjoint—the migration operator. These methods usually take the form of two approaches—for preconditioning before least-squares migration and as a single operation to improve accuracy of a conventionally migrated image. Previously, this has been done by migration deconvolution (Hu et al., 2001; Yu et al., 2006), approximating the diagonal of \mathbf{H}^{-1} to account for amplitude effects (Rickett, 2003; Sacchi et al., 2007), and by finding and applying a bank of non-stationary matching filters (Guitton, 2004, 2017) or deblurring filters (Aoki and Schuster, 2009) to a conventionally migrated image. This traditionally is done using a sliding window approach, where windowed regions and partial overlap regions are specified, and different matching filters are specified in each region (Schuster, 2017).

In this paper, we take a different approach. We note that the two primary differences between least squares migrated images and conventional migrated images are amplitude and frequency variations (Hou and Symes, 2015, 2016). Here, we treat this as a data matching problem between two conventionally migrated images, and find separate operations to account for both amplitude and frequency variations.

This approach enables us to rely on local seismic attributes to measure and apply amplitude and frequency balancing operations instead of using a sliding window approach (Fomel, 2007a). This allows for the smooth estimation and application of these matching operations instead of applying them in discrete windows. Since the operations for balancing amplitude and frequency content are calculated and applied separately from each another, the effect of each operation can be adjusted independently, which is another advantage of the proposed method. To test the

proposed approach, we apply this method to an example of reverse-time migration on the Sigsbee synthetic data set (Paffenholz et al., 2002).

THEORY

The goal of least-squares migration is to find the image, $\hat{\mathbf{r}}$, that minimizes

$$p(\hat{\mathbf{r}}) = \frac{1}{2} \|\mathbf{d} - \mathbf{L}\hat{\mathbf{r}}\|_2^2 , \quad (4.1)$$

where \mathbf{L} is the forward modeling operator, representing seismic wave propagation through the subsurface, and \mathbf{d} is the acquired seismic data. This can be solved by the least-squares formulation to find $\hat{\mathbf{r}}$:

$$\hat{\mathbf{r}} = (\mathbf{L}^\top \mathbf{L})^{-1} \mathbf{L}^\top \mathbf{d} , \quad (4.2)$$

where the migration operator, \mathbf{L}^\top , is adjoint to the forward modeling operator and is typically sparse, and $(\mathbf{L}^\top \mathbf{L})^{-1}$ is the inverse Hessian operator. Equation (4.2) is usually solved iteratively, typically requiring multiple iterations of forward modeling and remigrating the seismic image (Kuehl and Sacchi, 2003; Xue et al., 2016). Conventional migration is less computationally expensive:

$$\mathbf{m}_0 = \mathbf{L}^\top \mathbf{d}. \quad (4.3)$$

However, conventionally migrated images generally exhibit less correct amplitude and frequency content than least-squares migrated images (Dutta et al., 2014). By combining equations (4.2) and (4.3), it is evident that

$$\hat{\mathbf{r}} = (\mathbf{L}^\top \mathbf{L})^{-1} \mathbf{m}_0 , \quad (4.4)$$

so \mathbf{m}_0 is a distorted version of $\hat{\mathbf{r}}$, and $\hat{\mathbf{r}}$ can be recovered from \mathbf{m}_0 by finding a good approximation of $(\mathbf{L}^\top \mathbf{L})^{-1}$.

METHOD

In order to approximate $(\mathbf{L}^T \mathbf{L})^{-1}$, we follow the modeling and remigration process of Guittot (2004). We begin by forward modeling the migrated image, \mathbf{m}_0 :

$$\mathbf{d}_1 = \mathbf{L}\mathbf{m}_0 . \quad (4.5)$$

We then remigrate \mathbf{d}_1 :

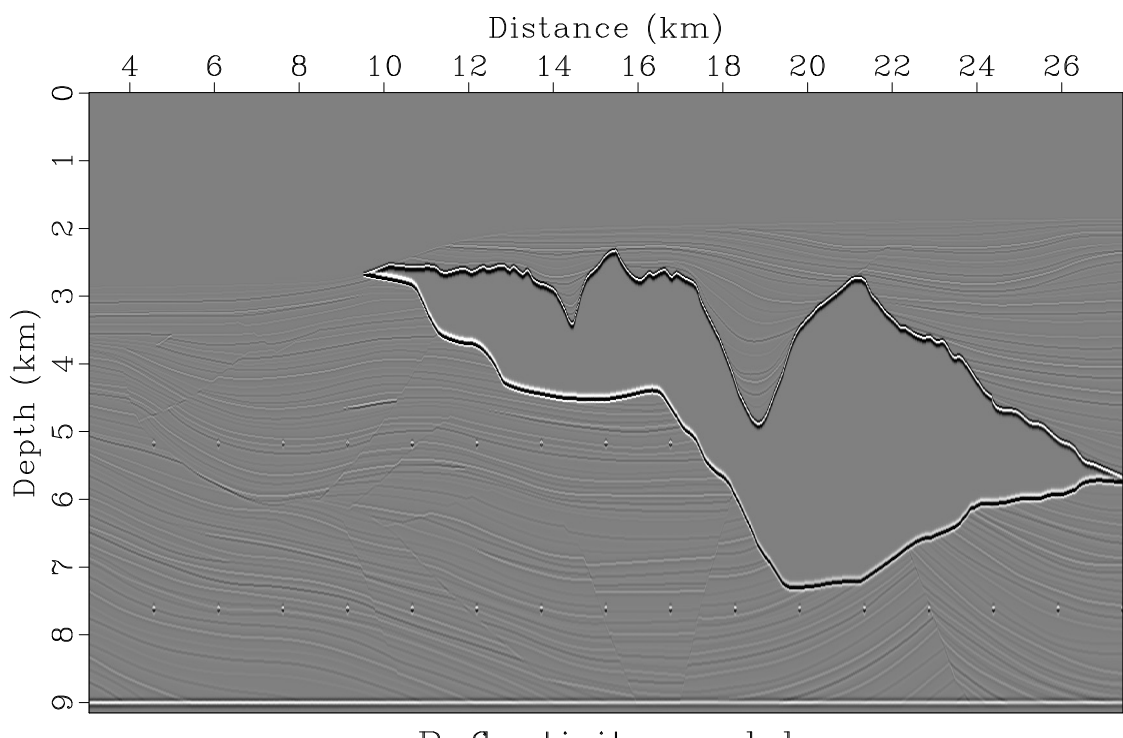
$$\mathbf{m}_1 = \mathbf{L}^T \mathbf{d}_1 = (\mathbf{L}^T \mathbf{L}) \mathbf{m}_0 , \quad (4.6)$$

and then find the operator, $(\mathbf{L}^T \mathbf{L})^{-1}$, that satisfies

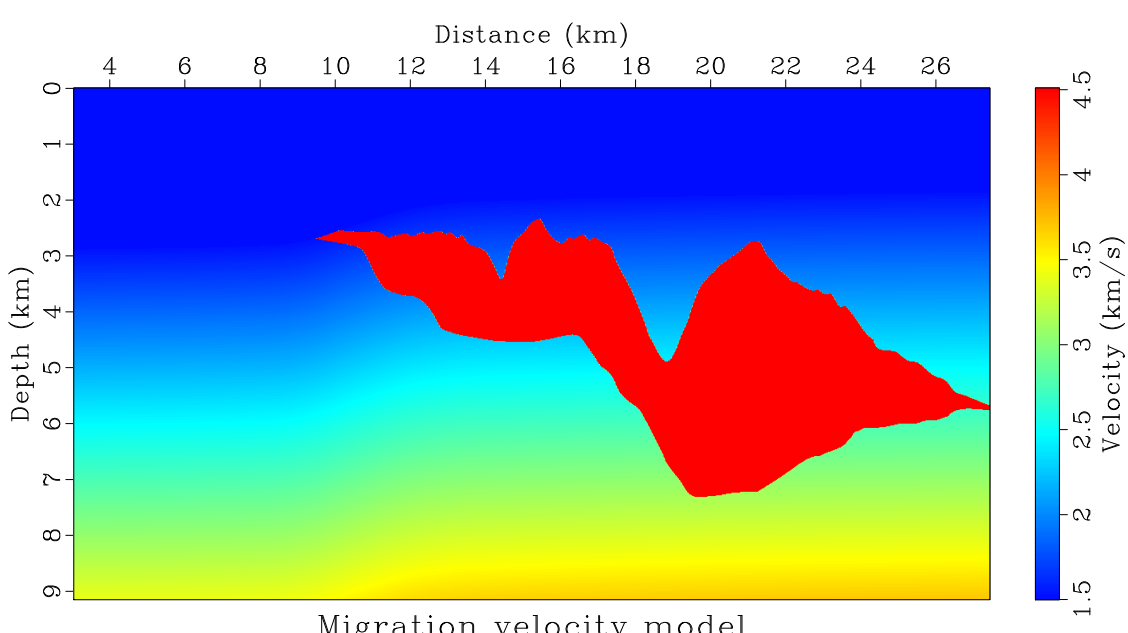
$$\mathbf{m}_0 = (\mathbf{L}^T \mathbf{L})^{-1} \mathbf{m}_1 . \quad (4.7)$$

Therefore, the inverse Hessian operator, $\mathbf{H}^{-1} = (\mathbf{L}^T \mathbf{L})^{-1}$, that must be applied to \mathbf{m}_0 to get $\hat{\mathbf{r}}$ can be calculated by first finding the transformation, \mathbf{H} , that maps \mathbf{m}_0 to \mathbf{m}_1 , and then inverting it. This can be interpreted as a data matching problem between \mathbf{m}_1 and \mathbf{m}_0 .

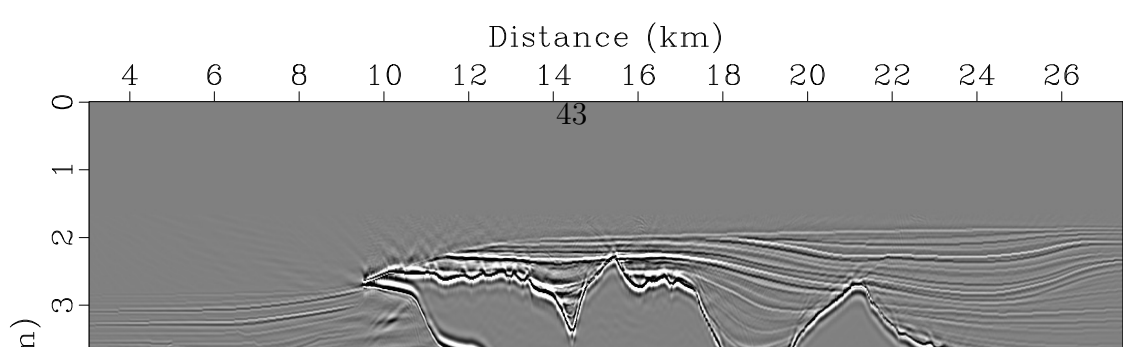
Since the primary differences between conventionally migrated images and least-squares migrated images amount to amplitude and frequency variations, we use two separate non-stationary operators to represent the forward Hessian—one to account for amplitude variations, and the other to account for frequency variations. Therefore, our approximation of \mathbf{H} can be calculated from some application of a non-stationary amplitude balancing operator, \mathbf{A} , and a non-stationary frequency balancing operator, \mathbf{S} . We first calculate the forward Hessian since the forward frequency balancing operation, \mathbf{S} , is well defined and simple to calculate. We then invert our approximation to the Hessian and apply it to \mathbf{m}_0 to correct the amplitude and frequency content of the migrated image.



(a)



(b)



Amplitude operator

First, we choose to find an amplitude balancing operation that, when applied to \mathbf{m}_0 , balances the amplitudes of \mathbf{m}_0 with respect to \mathbf{m}_1 . This operation can be equated to a trace-by-trace multiplication of a diagonal matrix to each trace, where the matrix changes for every trace. We estimate it by first calculating the amplitude envelope of the traces in \mathbf{m}_0 and \mathbf{m}_1 , and then smoothly dividing them. The corresponding diagonal weighting operator, \mathbf{A} , can be applied such that $\mathbf{m}_1 \approx \mathbf{A}\mathbf{m}_0$ to balance the amplitudes of each trace. Since this is a linear operation that only has diagonal elements, it is trivial to find the inverse operator, \mathbf{A}^{-1} .

Frequency operator

In addition to amplitude corrections, we also attempt to account for the decrease in resolution of a conventional migrated image compared to its corresponding least-squares migrated image. This loss in resolution can be equated to the fact that $\mathbf{L}^\top \mathbf{L}$ acts as a blurring operator, where the conventional migrated image is a blurred version of the ideal least-squares migrated image (Hu et al., 2001). We choose to approximate this blurring using non-stationary triangle smoothing.

We begin by first calculating the local frequency of the two initial images (Fomel, 2007a). Local frequency is a temporally and spatially varying frequency attribute that smoothly varies across the image without windows. Our goal is to find a transformation that we can apply to \mathbf{m}_0 that matches the local frequency content with \mathbf{m}_1 . To do this, we propose using non-stationary triangle smoothing. This approach involves finding and applying a non-stationary smoothing operator, which is the amount of samples, in both dimensions, that \mathbf{m}_0 will be averaged over in a

triangle weight, to balance the local frequency content with \mathbf{m}_1 .

We find the smoothing radius iteratively using the method of Greer and Fomel (2017), with a modification that allows the smoothing radius to be calculated in both spatial directions. Essentially, this is found by choosing an initial guess of a smoothing radius, $\mathbf{R}^{(0)}$, and updating it iteratively such that

$$\mathbf{R}^{(i+1)} = \mathbf{R}^{(i)} + \alpha [\mathbf{F}[\mathbf{S}_{\mathbf{R}^{(i)}} \mathbf{m}_0] - \mathbf{F}[\mathbf{m}_1]] , \quad (4.8)$$

where \mathbf{F} is the local frequency operator, $\mathbf{S}_{\mathbf{R}^{(i)}}$ is the smoothing operator of radius \mathbf{R} at the i th iteration, and α is a scalar constant that represents the step length. After a small number of iterations, the smoothing operator is found that, once applied to \mathbf{m}_0 , balances local frequency content with \mathbf{m}_1 .

Calculating the inverse Hessian

Now that we have found the forward operators that separately balance amplitude and frequency content from \mathbf{m}_0 to \mathbf{m}_1 , where $\mathbf{m}_1 \approx \mathbf{H}\mathbf{m}_0$, we want to find what combination of \mathbf{A} and \mathbf{S} best approximates \mathbf{H} . Since $\mathbf{H} = \mathbf{L}^T \mathbf{L}$ is symmetric, we want our approximation of \mathbf{H} to be as close to symmetric as possible. Therefore, we define \mathbf{H} as

$$\mathbf{H} \approx \mathbf{A}^{1/2} \mathbf{S} \mathbf{A}^{1/2} , \quad (4.9)$$

where \mathbf{A} is the operator that balances the amplitudes of \mathbf{m}_0 with respect to \mathbf{m}_1 , and \mathbf{S} is the operator that balances the local frequency content of \mathbf{m}_0 with respect to \mathbf{m}_1 , both defined previously. Applying the operations in this order allows the approximation of \mathbf{H} to be symmetric, since both \mathbf{A} and \mathbf{S} are symmetric operations. Splitting up our approximation to the Hessian into two separate operators allows us to control how much of each operation and the order of each operation goes into

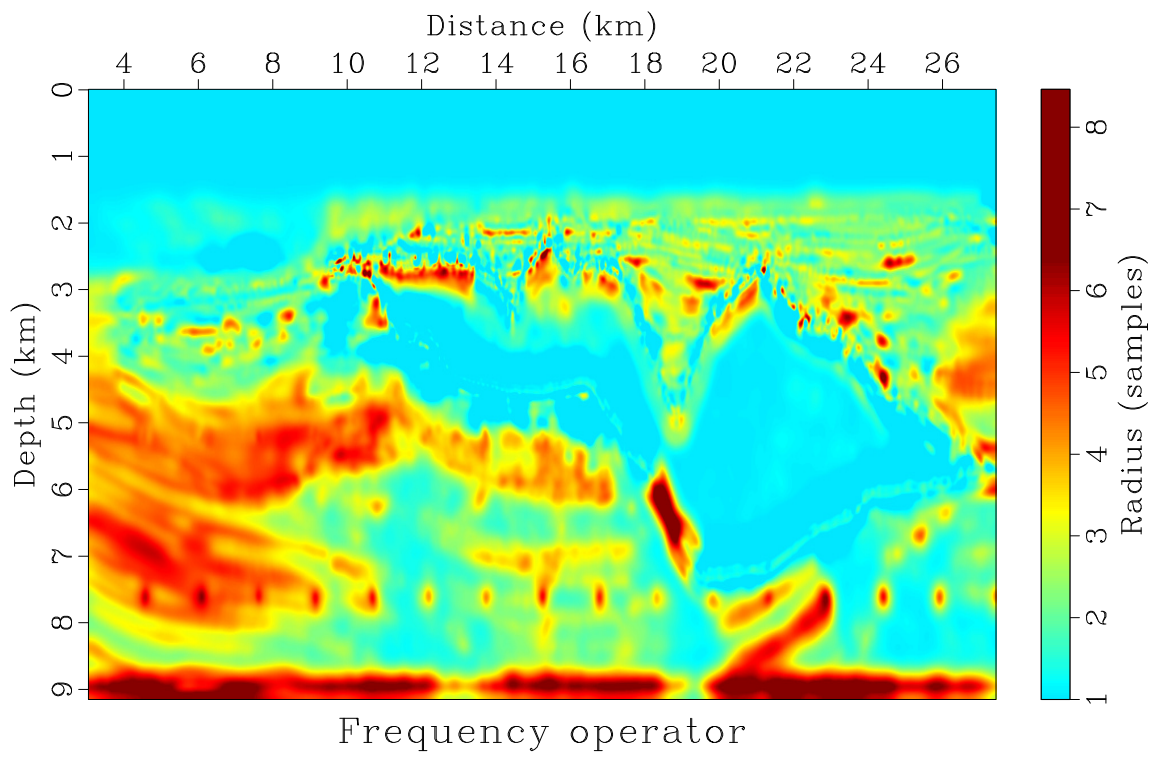
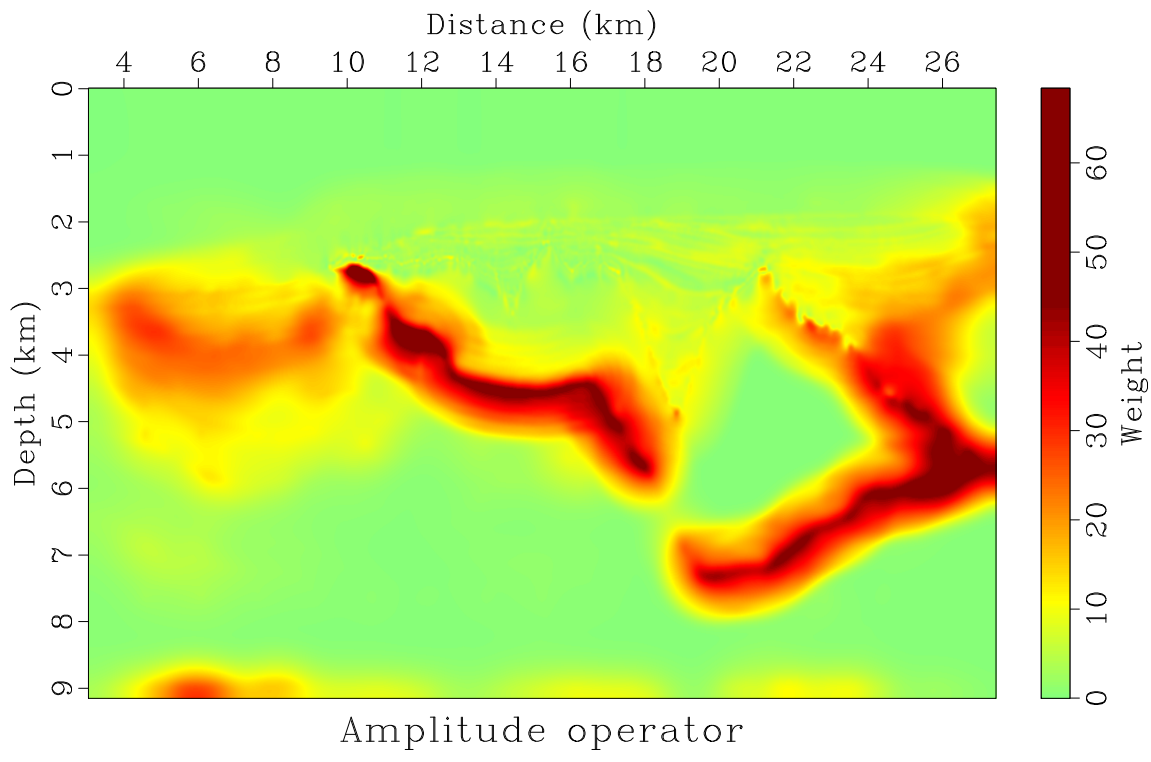


Figure 4.2: The forward amplitude balancing weight, \mathbf{A} (a) and the smoothing radius (b), which represents the number of samples in both dimensions that \mathbf{m}_0 must be smoothed over in a triangle weight to balance the local frequency content with \mathbf{m}_1 . This represents the forward smoothing operation, \mathbf{S} .

chapter-mighes/sigsbee a0,rect10b

correcting the image, and see how it affects the resulting image. Now that we have found the forward Hessian, \mathbf{H} , such that $\mathbf{H}\mathbf{m}_0 \approx \mathbf{m}_1$ using data matching operators, we want to find the inverse of this operator, \mathbf{H}^{-1} , such that $\hat{\mathbf{r}} \approx \mathbf{H}^{-1}\mathbf{m}_0$ provides us with the least-squares image. This is found as

$$\mathbf{H}^{-1} \approx (\mathbf{A}^{1/2} \mathbf{S} \mathbf{A}^{1/2})^{-1} = \mathbf{A}^{-1/2} \mathbf{S}^{-1} \mathbf{A}^{-1/2}. \quad (4.10)$$

Since the amplitude operators only contain diagonal terms, they are simple to invert. However, \mathbf{S}^{-1} is non-trivial to calculate since inverse smoothing can create physically unrealistic high-frequency data if inverted incorrectly without regularization. Therefore, \mathbf{S}^{-1} must be calculated with care to ensure the inverted data is physically plausible. We iteratively invert \mathbf{S} using shaping regularization (Fomel, 2007b), where the shaping operator is a bandpass filter picked to ensure the passband contains only physically possible frequencies for the given data set. The cost of applying our approximation to \mathbf{H}^{-1} in equation (4.10) is $\mathcal{O}(N)$, where N is the image size. The constant is small, typically around 10 for the number of iterations, and the calculation and application of this approximation is computationally insignificant compared to one iteration of least-squares migration.

EXAMPLE

We demonstrate the effectiveness of this method on the 2D Sigsbee model. The Sigsbee2A 2D synthetic data set was created to mimic the geology of the Sigsbee escarpment in the Gulf of Mexico (Paffenholz et al., 2002). A fixed-spread acquisition survey is generated, which consists of 301 shots spaced every 122 m. The source wavelet for generating the synthetic data is a Ricker wavelet centered at 10 Hz. The

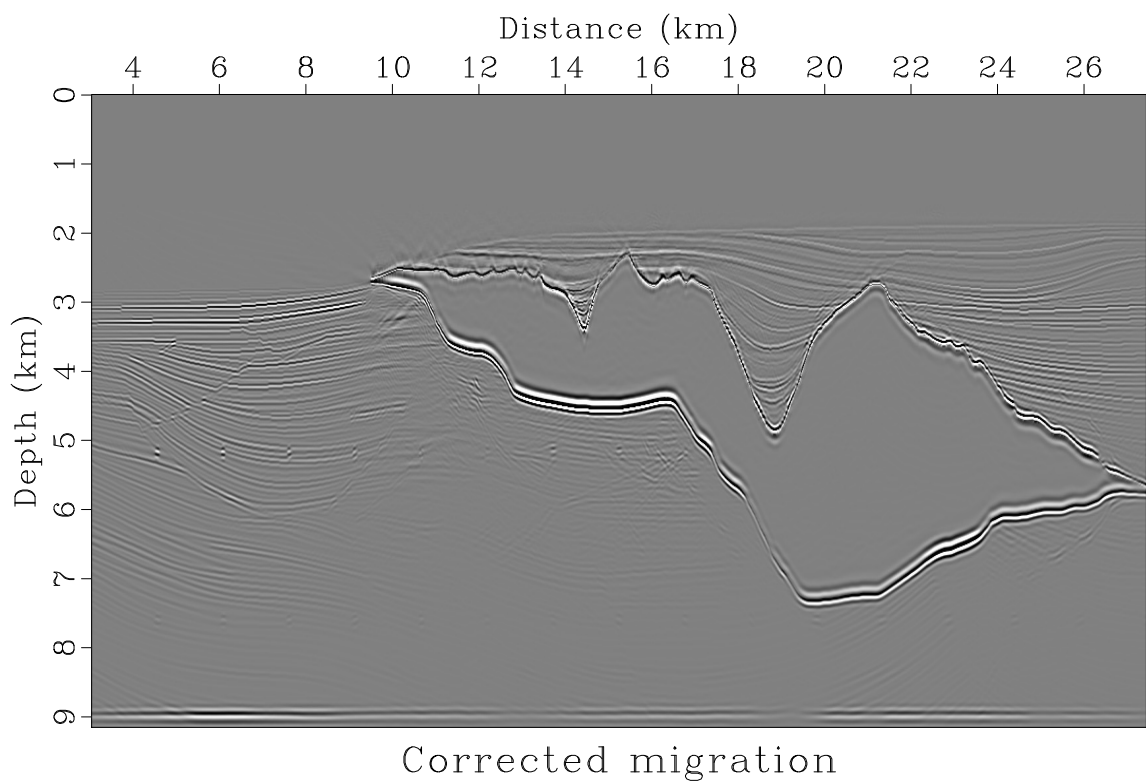
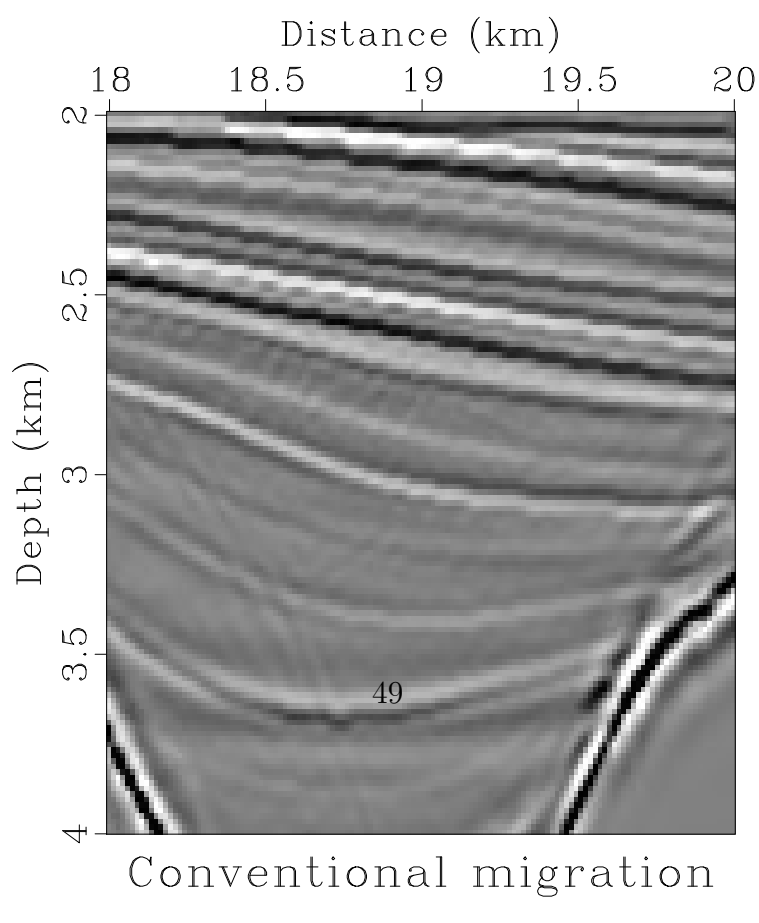
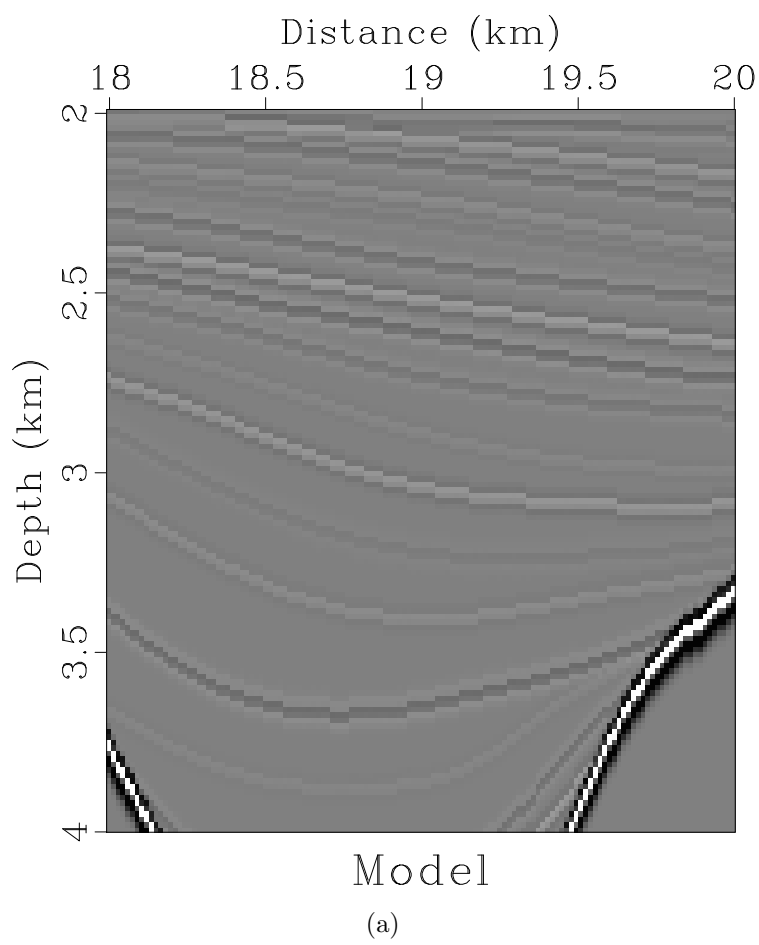


Figure 4.3: The corrected migrated image, found by applying equation (4.10) to \mathbf{m}_0 .
chapter-mighes/sigsbee migdec-shap



record length of the synthetic data is 10 s with a time step of 4 ms. We use reverse-time migration (RTM) as our migration operator.

We begin with the sub-surface reflectivity model (Figure 4.1(a)) and migration velocity model (Figure 4.1(b)). Next, we forward model the seismic data and migrate it to get our first conventionally migrated image, \mathbf{m}_0 (Figure 4.1(c)). Then, we forward model \mathbf{m}_0 and remigrate that data to get \mathbf{m}_1 (Figure 4.1(d)). This provides us with the two images, \mathbf{m}_0 and \mathbf{m}_1 , that we can use to find the operation \mathbf{H} that maps \mathbf{m}_0 to \mathbf{m}_1 .

Next, we calculate and apply the data matching operations as described in the previous section. The forward amplitude balancing weight, \mathbf{A} , is shown in Figure 4.2(a). The calculated radius for the forward smoothing operation is shown in Figure 4.2(b). After applying these two operators to \mathbf{m}_0 as described by equation (4.10), we produce the corrected migrated image, as shown in Figure 4.3. This corrected image better represents the subsurface reflectivity than the conventionally migrated image (Figure 4.1(c)), as it exhibits more correct amplitude content and higher resolution comparable with the reflectivity model.

Figure 4.4 shows a windowed section of the reflectivity model, the conventionally migrated image, and the corrected migrated image. The corrected migrated image exhibits clearly higher resolution and has more correct and consistent amplitude content than the conventionally migrated image.

In addition to directly applying this operator to the conventionally migrated image to improve resolution, this operator can be used as a preconditioner in iterative least-squares migration. In this case, the corrected migrated image could be used as an initial model for least-squares migration for faster convergence.

CONCLUSIONS

Least-squares migration can produce an accurate migrated image, but it is more computationally expensive than conventional migration. In this paper, we apply an approximate inverse Hessian operator to a conventional migrated image to approximate the least-squares migrated image. Since the primary differences between least-squares migration and conventional migration amount to amplitude and frequency variations, we approximate the forward Hessian by calculating frequency and amplitude matching operators. The amplitude matching operator is found by calculating the amplitude envelopes of migrated and remigrated images and smoothly dividing them, and the frequency matching operator is found using an iterative algorithm and non-stationary smoothing. The Hessian is approximated by a combination of these two operators to ensure symmetry. This method involves a windowless approach and is cheap to calculate and apply. Additionally, by defining the Hessian with two separate operators, we can examine, and control, the “ingredients” of the Hessian operator, and see how changing them impacts the final image.

After the forward Hessian is calculated, we invert it iteratively using shaping regularization, and apply it to the conventionally migrated image to get an approximation of the least-squares migrated image. Successful results are achieved on the 2D Sigsbee synthetic model with reverse-time migration as the migration operator.

ACKNOWLEDGEMENTS

We thank the sponsors of the Texas Consortium for Computational Seismology (TCCS) for their financial support. The examples in this paper can be reproduced using the Madagascar open-source software package (Fomel et al., 2013).

Chapter 5

Conclusions

Bibliography

- Al-Inaizi, S., R. Bridle, and N. Nakhla, 2004, Comparison of pre and post-stack super-merge of ten 3D blocks: Presented at the SEG Technical Program Expanded Abstracts 2004, Society of Exploration Geophysicists.
- Aoki, N., and G. T. Schuster, 2009, Fast least-squares migration with a deblurring filter: *GEOPHYSICS*, **74**, WCA83–WCA93.
- Carter, D., and S. Pambayuning, 2009, Extended bandwidth by a frequency domain merge of two 3D seismic volumes: *The Leading Edge*, **28**, 386–386.
- Claerbout, J. F., 1992, *Earth Soundings Analysis: Processing Versus Inversion*: Blackwell Scientific Publications.
- Dai, W., and G. T. Schuster, 2013, Plane-wave least-squares reverse-time migration: *GEOPHYSICS*, **78**, S165–S177.
- Dong, S., J. Cai, M. Guo, S. Suh, Z. Zhang, B. Wang, and Z. Li, 2012, Least-squares reverse time migration: towards true amplitude imaging and improving the resolution: Presented at the SEG Technical Program Expanded Abstracts 2012, Society of Exploration Geophysicists.
- Dutta, G., Y. Huang, W. Dai, X. Wang, and G. T. Schuster, 2014, Making the most out of the least (squares migration): 84th Annual International Meeting, SEG, Expanded Abstracts, 4405–4410.
- Fomel, S., 2007a, Local seismic attributes: *Geophysics*, **72**, A29–A33.
- , 2007b, Shaping regularization in geophysical-estimation problems: *GEOPHYSICS*, **72**, R29–R36.
- Fomel, S., M. Backus, K. Fouad, B. Hardage, and G. Winters, 2005, A multistep

approach to multicomponent seismic image registration with application to a West Texas carbonate reservoir study: 75th Ann. Internat. Mtg, Soc. of Expl. Geophys., 1018–1021.

Fomel, S., and M. M. Backus, 2003a, Multicomponent seismic data registration by least squares: 73rd Annual International Meeting, Soc. of Expl. Geophys., 701–784.

—, 2003b, Multicomponent seismic data registration by least squares: Presented at the SEG Technical Program Expanded Abstracts, Society of Exploration Geophysicists.

Fomel, S., and L. Jin, 2009, Time-lapse image registration using the local similarity attribute: *Geophysics*, **74**, A7–A11.

Fomel, S., P. Sava, I. Vlad, Y. Liu, and V. Bashkardin, 2013, Madagascar: open-source software project for multidimensional data analysis and reproducible computational experiments: *Journal of Open Research Software*, **1**, e8.

Fomel, S. G. S., 2018, Matching and merging high-resolution and legacy seismic images: *GEOPHYSICS*, **83**, V115V122.

Greer, S., and S. Fomel, 2017, Balancing local frequency content using non-stationary smoothing: Presented at the 87th Ann. Internat. Mtg, Soc. of Expl. Geophys. (Submitted).

Guitton, A., 2004, Amplitude and kinematic corrections of migrated images for nonunitary imaging operators: *GEOPHYSICS*, **69**, 1017–1024.

—, 2017, Fast 3D least-squares RTM by preconditioning with nonstationary matching filters: Presented at the SEG Technical Program Expanded Abstracts 2017, Society of Exploration Geophysicists.

Hale, D., 2013, Dynamic warping of seismic images: *GEOPHYSICS*, **78**, S105–S115.

- Hardage, B. A., M. V. DeAngelo, P. E. Murray, and D. Sava, 2011, Multicomponent seismic technology: Society of Exploration Geophysicists.
- Herrera, R. H., S. Fomel, and M. van der Baan, 2014, Automatic approaches for seismic to well tying: *Interpretation*, **2**, SD9–SD17.
- Herrera, R. H., and M. van der Baan, 2012, Guided seismic-to-well tying based on dynamic time warping: 82nd Annual International Meeting, Society of Exploration Geophysicists, 1–5.
- Hestenes, M. R., and E. Stiefel, 1952, Methods of Conjugate Gradients for Solving Linear Systems: *Journal of Research of the National Bureau of Standards*, **49**, 409–436.
- Hou, J., and W. Symes, 2016, Accelerating least squares migration with weighted conjugate gradient iteration: Presented at the 78th EAGE Conference and Exhibition 2016, EAGE Publications BV.
- Hou, J., and W. W. Symes, 2015, An approximate inverse to the extended born modeling operator: *GEOPHYSICS*, **80**, R331–R349.
- Hu, J., G. T. Schuster, and P. A. Valasek, 2001, Poststack migration deconvolution: *GEOPHYSICS*, **66**, 939–952.
- Kuehl, H., and M. D. Sacchi, 2003, Least-squares wave-equation migration for AVP/AVA inversion: *Geophysics*, **68**, 262–273.
- Liu, Y., and S. Fomel, 2012, Seismic data analysis using local time-frequency decomposition: *Geophysical Prospecting*, **61**, 516–525.
- Lumley, D., D. C. Adams, M. Meadows, S. Cole, and R. Wright, 2003, 4D seismic data processing issues and examples: 73rd Annual International Meeting, Society of Exploration Geophysicists, 1394–1397.
- Meckel, T., N. L. Bangs, and T. Hess, 2017, 3D multichannel seismic field data from

the San Luis Pass region off Galveston, Texas, acquired by the R/V Brooks-McCall in 2013 (BM1310).

Meckel, T. A., and F. J. Mulcahy, 2016, Use of novel high-resolution 3D marine seismic technology to evaluate Quaternary fluvial valley development and geologic controls on shallow gas distribution, inner shelf, Gulf of Mexico: Interpretation, **4**, SC35–SC49.

Mohan, T. R. M., C. B. Yadava, S. Kumar, K. K. Mishra, and K. Niyogi, 2007, Prestack merging of land 3D vintages — a case history from Kavery Basin, India: Presented at the SEG Technical Program Expanded Abstracts 2007, Society of Exploration Geophysicists.

Paffenholz, J., B. McLain, J. Zaske, and P. Keliher, 2002, Subsalt multiple attenuation and imaging: Observations from the Sigsbee2b synthetic dataset: 72nd Annual International Meeting, SEG, Expanded Abstracts, 2122–2125.

Petersen, C. J., S. Buenz, S. Hustoft, J. Mienert, and D. Klaeschen, 2010, High-resolution P-Cable 3D seismic imaging of gas chimney structures in gas hydrated sediments of an Arctic sediment drift: Marine and Petroleum Geology, **27**, 1981–1994.

Phillips, M., and S. Fomel, 2016, Seismic time-lapse image registration using amplitude-adjusted plane-wave destruction: SEG Technical Program Expanded Abstracts, Society of Exploration Geophysicists, 5473–5478.

Rickett, J. E., 2003, Illumination-based normalization for wave-equation depth migration: GEOPHYSICS, **68**, 1371–1379.

Ross, C. P., and M. S. Altan, 1997, Time-lapse seismic monitoring: Some shortcomings in nonuniform processing: The Leading Edge, **16**, 931–937.

Sacchi, M. D., J. Wang, and H. Kuehl, 2007, Estimation of the diagonal of the mi-

- gration blurring kernel through a stochastic approximation: Presented at the SEG Technical Program Expanded Abstracts 2007, Society of Exploration Geophysicists.
- Schuster, G. T., 2017, Seismic inversion: Society of Exploration Geophysicists.
- Ursenbach, C., P. Cary, and M. Perz, 2013, Limits on resolution enhancement for PS data mapped to PP time: *The Leading Edge*, **32**, 64–71.
- White, R. E., 1991, Properties of instantaneous seismic attributes: *The Leading Edge*, **10**, 26–32.
- Xue, Z., Y. Chen, S. Fomel, and J. Sun, 2016, Seismic imaging of incomplete data and simultaneous-source data using least-squares reverse-time migration with shaping regularization: *Geophysics*, **81**, no. 1, S11–S20.
- Yu, J., J. Hu, G. T. Schuster, and R. Estill, 2006, Prestack migration deconvolution: *GEOPHYSICS*, **71**, S53–S62.
- Zhou, J., J. Sun, and X. Ma, 2014, Application of Gabor transform to amplitude spectrum matching for merging seismic surveys: Presented at the SEG Technical Program Expanded Abstracts 2014, Society of Exploration Geophysicists.